Aging and Disease
www.aginganddisease.org
Early access date: June 24, 2026
http://dx.doi.org/10.14336/AD.2026.0213

Origianl Article

Staging of Neuropil Morphological Alterations in Alzheimer's Disease

Zhi-Yi Zhang[1,2#], Xin-Meng Wang[3,4#], Xin Ma[5], Yi Wang[6], Shuai-Deng Wang[1,2], Yi-Lin Peng[1,2], Kun Cheng[3,4], Yue-Ru Shen[2], Guo-Zhang Tang[5], Chen-Wei Wang[1,2,7*], Jiang-Ning Zhou[2]

[1]Department of Anatomy, School of Basic Medical Sciences, Anhui Medical University, Hefei 230032, Anhui, China. [2]Institute of Brain Science, the First Affiliated Hospital of Anhui Medical University, Hefei 230022, Anhui, China. [3]Department of Pharmacy, the First Affiliated Hospital of Anhui Medical University, Hefei 230022, Anhui, China. [4]School of Pharmacy, Anhui Medical University, Hefei 230032, Anhui, China. [5]Second School of Clinical Medicine, Anhui Medical University, Hefei 230032, Anhui, China [6]First School of Clinical Medicine, Anhui Medical University, Hefei 230032, Anhui, P. R. China. [7]Anhui Provincial Key Laboratory for Brain Bank Construction and Resource Utilization, Anhui Medical University, Hefei 230032, Anhui, China.

[Received February 14, 2026; Revised June 22, 2026; Accepted June 23, 2026]

ABSTRACT: Alzheimer's disease (AD) involves the progressive fragmentation of neural connectivity. This study aims to investigate the morphological degeneration of neuropil fibers in AD and evaluate their utility as a marker for pathological severity. Post-mortem brain tissues from 92 cases across eight distinct regions were analyzed. We used Bielschowsky silver staining with automated quantitative morphometry to measure neuritic fiber length and curvature in the neuropil, and immunofluorescence to detect neurite cytoskeletal markers. Finally, a novel histological staging system for neuropil disruption was established to assess disease progression. Morphometric analysis revealed progressive reductions in neuritic fiber length and increased curvature tracking with disease severity, a significant negative correlation confirmed these are coupled degenerative manifestations. Immunofluorescence demonstrated extensive cytoskeletal fragmentation that corresponded to the pattern observed with silver staining. Based on morphometric analysis, a novel four-tier staging system was established, defined neuropil by homogeneous compactness (-), initial (+), extensive (++) disruption, and complete fragmentation (+++), which correlated preferentially with Phospho-Tau load. Crucially, subtle neuropil alterations were detectable in the entorhinal cortex, amygdala, and anterior hippocampus even in Braak 0 stage, suggesting a potential association between these early changes and the initial stages of tau pathogenesis. This study establishes a staging system for assessing neuropil degeneration, demonstrating that neuropil fragmentation and geometric distortion are candidate AD pathological markers. By systematically analyzing neuritic fiber morphology and proposing a neuropil disruption stage, this work provides critical insights into early AD pathogenesis, offering a foundation for future diagnostic strategies pending validation in independent cohorts with clinical correlations.

Keywords: Alzheimer's disease, neurite, neuropil, Tau pathology

INTRODUCTION

As the most prevalent neurodegenerative disease and the leading cause of dementia globally, Alzheimer's disease (AD) is a progressive condition characterized by gradual cognitive decline and memory loss. AD is characterized by neuropil volume reduction [1], synaptic loss, the accumulation of amyloid-beta (Aβ) plaques, the abnormal hyperphosphorylation of tau protein leading to the formation of neurofibrillary tangles (NFTs) and Neuropil threads (NT) [2, 3]. In neuroscience, the term "neuropil" traditionally refers to the commingled substrate consisting

***Correspondence should be addressed to:** Dr. Chen-Wei Wang, Department of Anatomy, School of Basic Medical Sciences, Anhui Medical University, Hefei 230032, Anhui, P. R. China.Email: cwwang@ahmu.edu.cn. #These authors contributed equally to this work.

of axons, dendrites, and glial cells typically observed in the gray matter of the central nervous system [4, 5]. Among these the hyperphosphorylation of Tau protein, a critical early pathological hallmark of AD [6, 7], leads to synaptic dysfunction and drives axonal degeneration [8]. This disruption of neurite integrity underscores the necessity to investigate neuritic morphological alterations as a central event in AD pathogenesis, especially in the early stages.

Previous studies have shown that age-dependent structural defects of myelin promote Aβ plaque formation directly and indirectly and are therefore an upstream AD risk factor [9], and myelin-axon interface is a critical site of protein aggregation and disrupted neuro-glial signaling in AD [10]. Therefore, the integrity and morphological alterations of the axon itself, the core conductive unit ensheathed by myelin, may constitute a critical link connecting upstream myelin pathology to downstream neural circuit dysfunction and cognitive decline. However, most discussions on axonal pathology are focused on observations of presynaptic terminal degeneration under electron microscopy or the molecular mechanisms of transport impairments [11, 12]. Consequently, there remains a notable lack of systematic description of the changes in the overall geometric morphology of neurites, functioning as integral conductive units, across different stages of the disease.

Existing evidence has suggested significant disruption of axonal structure, it has been demonstrated that a greater average number of axonal spheroids per amyloid plaque and larger plaque-associated axonal spheroids size in individuals with moderate to severe AD, compared with those with mild cognitive impairment [13]. Researchers also have observed that during the progression of AD, the proportion of abnormally myelinated axons increases stepwise, with AD cases exhibiting a significantly higher percentage compared to both no cognitive impairment and mild cognitive impairment [14]. MRI and fluid biomarkers revealed higher levels of NF-L and GFAP were associated with lower total brain axonal density, and axonal density may decline globally in relation to non-specific processes such as neuronal injury or astrogliosis, yet decline regionally in relation to AD neurodegenerative processes, particularly in cognitively unimpaired individuals [15]. These results collectively indicate that reduced axonal density is strongly associated with the pathological process of AD, which further underscores the necessity of investigating axonal morphology.

To contextualize these morphological insights, it is necessary to evaluate them against established staging frameworks which traditionally prioritize the topography of protein aggregates. The Braak staging system, based on the predictable topographic spread of phosphorylated tau (pTau) pathology, provides a robust framework for classifying disease progression, wherein NFTs are first seen in a few limbic cortical areas, and from here the destructive process spreads in a predictable, non-random manner across the cortex and brain stem [16]. While it effectively delineates a “diffusion map” of tau pathology across macro-scale brain networks, the corresponding alterations in neuritic morphology remain to be fully integrated into this topographic framework. Which could help reveal regional neuropil damage patterns that may not be apparent from single AD marker.

This study therefore aimed to delineate the spatiotemporal trajectory of neuropil fibers degeneration within the neuropil across Braak stages in AD, through an integrated approach combining multi-scale quantitative morphological analysis with a novel assessment of neuropil structural integrity.

MATERIALS AND METHODS

Cohort selection

In this study, autopsy brain tissue was obtained from three different institutions and the sampling of the blocks was carried out by experienced neuropathologists. Samples were obtained from donors of two ethnic backgrounds: East Asian and European. For the East Asian cohort, 11 donors were recruited from the National Health and Disease Human Brain Tissue Resource Center (Anhui Medical University, Hefei, China), and 50 donors were obtained from the National Human Brain Bank for Development and Function (Chinese Academy of Medical Sciences and Peking Union Medical College, Beijing, China), these two brain banks are hereinafter referred to as the China Brain Bank. For the European cohort, 31 donors were acquired from the Netherlands Brain Bank (Amsterdam, Netherlands). In this cohort of 92 cases, neuropathological evaluations, including the CERAD protocol [17], Braak NFT stage, Thal Plaque Phase [18, 19], were conducted on anatomical regions sampled in accordance with current NIA-AA consensus criteria and standard neuropathological practices. The demographics of the cases are given in Supplementary Table 1 and Supplementary Table 2. A total of 61 sets of 5 μm thick sections were produced from the following eight brain regions of 61 samples from China Brain Bank: Entorhinal Cortex (EC), Amygdala (Amy), anterior Hippocampus (aHipp), body of Hippocampus (bHipp), Middle Temporal Gyrus (MTG), Middle Frontal Gyrus (MFG), Inferior Parietal Lobule (IPL), Occipital Cortex (OCC). And 31 samples from Netherlands Brain Bank were sliced using only the MTG.

AD human brain paraffin brain sections were obtained from the Netherlands Brain Bank (coordinator:

Dr. Inge Huitinga), National Health and Disease Human Brain Tissue Resource Center (Anhui Medical University, Hefei, China) and National Human Brain Bank for Development and Function (Chinese Academy of Medical Sciences and Peking Union Medical College, Beijing, China). The study protocols involving human brain tissue samples were approved by the ethics committee of Anhui Medical University (No. 83244549), ethics committee of the Institute of Basic Medical Sciences, Chinese Academy of Medical Sciences (No. 2022125). All patients' identities were protected by de-identifying tissue samples, ensuring they could not be traced back to the donors.

Silver staining

This study employed the Bielschowsky silver staining method [20], as follows: processed sections were immersed in 20% silver nitrate at 37 °C for 20 min in the dark, then rinsed in distilled water for 10 min. Subsequently, sections were immersed in the 20% ammoniacal silver at room temperature in the dark for 20 min, then rinsed in a mixture of ammonium hydroxide and distilled water. Slides were placed in a solution containing formalin (20 ml), citric acid (0.5 g), concentrated nitric acid (2 drops), and distilled water (up to 100 ml), mixed with ammonium hydroxide in equal amounts, with continuous observation of staining until completion. After rinsing in distilled water, slides were immersed in 5% sodium thiosulfate solution for 5 min, then rinsed in distilled water for 5 min. After completion of the staining procedures, sections were rehydrated in ascending concentrations of ethanol (30%, 50%, 70%, and 96%) for 5 min each, cleared in two changes of xylene for 5 min each, and mounted with coverslips.

Immunofluorescent staining

Five-µm sections were deparaffinized and incubated in 0.5% PBST for 1 h, washed with PBS, then treated in Citrate-citric acid buffer for about 20 min in epitope retriever. Subsequently, sections were blocked with 5% normal donkey serum (017-000-121, Jackson Immuno Research, USA) in 0.5% PBST at 37C for 1 h. Sections were then incubated with primary antibody for 1 h at 37 °C, followed by overnight incubation at 4 °C. Primary antibody combinations used were rabbit anti-Myelin Basic Protein (MBP) (M3821, Sigma-Aldrich, USA, 1:1500) and mouse anti-Phospho-Tau (Ser202, Thr205) Monoclonal (AT8) (MN1020, Thermo Fisher, USA, 1:1500); rabbit anti-Neurofilament 200 (NF-H) (N4142, Sigma-Aldrich, USA, 1:1500) and mouse anti-neurofilament light polypeptide (NF-L) (60189-1-Ig, Proteintech, USA, 1:1000). To validate antibody specificity and distinguish genuine target staining from background, negative controls were included for each experiment by omitting the primary antibodies (secondary antibody-only controls) or by replacing them with species-matched non-immune IgG (isotype controls) at the same concentration, healthy human brain sections were employed as tissue plus controls and incubated with the primary antibodies (Supplementary Fig. 1). The sections were then washed three times with PBS and incubated in secondary antibody in blocking buffer 1:200 for 2 hours at room temperature. Secondary antibodies used were donkey anti-mouse (715-585-151, Jackson, USA) for AT8 and NF-L; donkey anti-rabbit (711-545-152, Jackson, USA) for MBP and NF-H. After rinsing with PBS three times, the sections were incubated in DAPI (1:2000) for 10 minutes and mounted with coverslips.

Immunohistochemistry

For Immunohistochemistry, 5-µm sections were deparaffinized and incubated in 0.5% PBST for 1 h, washed with PBS, then treated in Citrate-citric acid buffer for about 20 min in epitope retriever. Subsequently, sections were blocked with 5% normal donkey serum (017-000-121, Jackson Immuno Research, USA) in 0.5% PBST at 37C for 1 h. Sections were then incubated with mouse anti-Phospho-Tau (Ser202, Thr205) Biotin Monoclonal (AT8) (MN1020B, Thermo Fisher, USA, 1:200) for 1 h at 37 °C, followed by overnight incubation at 4 °C. Subsequently, sections were incubated with biotinylated horse anti-mouse IgG (BA-2000, Vector Laboratories, USA, 1:200) and an avidin-biotin peroxidase complex (PK-4000, Vector Laboratories, USA, 1:200). Sections were developed with 0.05% 3,3'-diaminobenzidine (Sigma-Aldrich, USA) as chromogen. All sections were counterstained with hematoxylin, then rehydrated with ethanol at ascending concentrations (30, 50, 70, and 96%) for 5 min each, cleared in two changes of xylene for 5 min each, and mounted with coverslips.

Image Acquisition and Region of Interest Selection

To analyze the length and curvature of horizontal and vertical neuropil fibers, 31 donors were selected from the Netherlands Brain Bank, specifically focusing on the MTG. Using 5-µm-thick paraffin-embedded human brain sections, whole-slide images were acquired using the VS200 Slide Scanning Microscope System (Olympus, Japan) at 40× magnification. For quantitative analysis, a circular region of interest (ROI) with a diameter of 200 µm was defined to simulate the field of view under a microscope configuration using a 100× objective lens and an eyepiece with a field number of 20 mm (e.g., a 10×/20

eyepiece). In practice, varying numbers of MTG brain samples slices were selected from each donor and subjected to staining, ROI selection, and evaluation. All selected ROIs were consistently located in cortical Layer III. For the fiber length analysis, we utilized samples slices from 31 donors, systematically evaluating 60– 80 sample slices per donor; two distinct ROIs were selected per sample slice, and approximately 100– 200 fibers were measured within each ROI. Similarly, for the fiber curvature analysis across the 31 donors, we assessed 5– 6 sample slices per donor, selecting two distinct ROIs per sample slice to measure 3– 6 fibers per ROI. In contrast, for the immunofluorescence intensity quantification, one representative ROI was selected and quantified from each slice, with three to six tissue slices analyzed for each individual donor. All image acquisition and ROI selection were conducted in a strictly blinded manner; investigators were blinded to clinical information (including Braak stage, APOE genotype, and clinical diagnosis). And slides were coded with randomized alphanumeric identifiers, then chose examples closest to group mean values for key parameters (e.g., fiber length, curvature, plaque density), avoiding outliers or atypical features.

Quantification of Fiber Orientation and Length

Neuropil fiber orientation was operationally determined relative to the surface of cortex. This assessment relied on a semi-automated algorithmic approach within ImageJ (version 1.54f). Based on this reference plane, "vertical" fibers were defined as those oriented roughly orthogonal to the cortical surface (90° ± 30°). On the other hand, "horizontal" fibers were classified as those running parallel to the cortical surface itself (0° ± 30°). Fibers with highly ambiguous orientation that could not be clearly categorized were excluded from the statistical analysis to ensure data stringency. To ensure rigorous quality control and mitigate potential observer bias, inter-rater reliability was qualitatively assessed and maintained through a mutual cross-validation protocol. Within each ROI, the length of all visible horizontal and vertical fibers was measured. The morphological quantification, focusing on fiber length and curvature, was evenly divided between two independent investigators (Z.Z. and X.M.). During the image processing in ImageJ, all tracing trajectories of the fibers were systematically saved. Subsequently, a cross-verification step was executed wherein the annotated trajectories generated by one researcher were independently reviewed by the other. This consensus-based approach was strictly implemented to ensure high accuracy and consistency in evaluating fiber morphological metrics, particularly in distinguishing fiber orientation.

Quantification of Fiber Curvature

For curvature analysis, a systematic spatial sampling strategy was employed to minimize bias: each ROI was geometrically divided into four quadrants, and the most centrally located fiber in each quadrant meeting inclusion criteria was selected for tracing. This method yielded 3 to 6 fibers per image, ensuring the mean curvature accurately reflected the global cytoskeletal curvature of the ROI rather than localized anomalies (Supplementary Fig. 2). The morphological curvature of neuritic fibers was determined using the "Kappa-Curvature Analysis" plugin in ImageJ. Mathematically, curvature (κ) is defined as the rate of change of the tangent angle with respect to arc length. The Kappa plugin reconstructs the continuous geometric morphology of the fiber by fitting the user-defined points to a B-spline curve. It then calculates the local curvature at each discrete point along the curve using the formula: $\kappa = \frac{|y''|}{(1+y'^2)^{3/2}}$, where y is the function defining the curve in the form $y(x)$ with y' and y'' representing its first and second derivatives with respect to x, respectively.

The physical distance parameters were first calibrated in ImageJ according to the image scale bar, followed by launching the "Kappa" plugin. Target fibers were selected and locally magnified. A high-density point-and-click tracing was then performed carefully along the neuritic fiber to ensure the most accurate representation of its true anatomical path. Once the tracing of a single fiber was completed, the fitted curve was generated. The system automatically calculates the local curvature for all sampled points along the fitted B-spline curve and outputs the mean value. Therefore, the final curvature data for each traced fiber in this study represents the arithmetic mean of the local curvatures of all points along that specific fiber.

Immunofluorescence Intensity Quantification

Immunofluorescence intensity was analyzed in the MTG of 16 demographically matched samples from the Netherlands Brain Bank. Samples were stratified into four groups based on disease progression: Braak stages I, IV, V, and VI. High-resolution images for this analysis were acquired using Spin SR microscopy (Olympus, Japan). Selection and quantification were performed by an investigator blinded to clinical and pathological metadata to ensure reproducibility.

Neuropil Alteration Staging Assessment

For the staging assessment of neuropil, 61 donors were obtained from the China Brain Bank. Assessments were

conducted across the following brain regions: EC, Amy, aHipp, bHipp, MTG, MFG, IPL, and OCC. To ensure the objective and reproducible application of the proposed four-stage neuropil disruption staging system, a standardized evaluation protocol was implemented. Prior to grading, all images were anonymized, randomized, and stripped of all identifying information. The staging was conducted by two independent assessors who were strictly blinded to the subjects' clinical information, Braak stages and APOE genotypes. Assessors evaluated the images based on predefined morphological criteria. The initial inter-rater reliability was substantial, yielding a Cohen's kappa of 0.80. In cases where the initial assigned stages differed between the two independent assessors, a consensus was reached through joint review and discussion. By employing this blinded, dual-assessor approach, we minimized subjective bias and confirmed that the staging criteria could be consistently and robustly applied across a heterogeneous cohort of human post-mortem cases.

Statistical Analysis

Given the inherent heterogeneity and unequal variances in human post-mortem tissue, before performing any group comparisons, the distribution of all datasets was formally assessed using the D'Agostino-Pearson omnibus normality test to evaluate both normality and lognormality. No estimable outcome showed a significant omnibus Braak stage × APOE genotype interaction in the donor-aware mixed-effects models (all $P \geq 0.195$; Supplementary Table 6), and the corresponding interaction effect estimates are reported in Supplementary Table 7. Therefore, no follow-up model-based pairwise contrasts were generated. An ordinary one-way analysis of variance (ANOVA) was utilized exclusively for the specific multi-group comparisons of morphological metrics (i.e., fiber length and average curvature) across multiple Braak stages. For all other analyses, which involved comparing only two groups, unpaired t-tests were employed for datasets that passed the normality test ($p > 0.05$). For datasets that did not follow a normal distribution, or in instances where the sample size was insufficient to reliably determine normality ($N < 6$), non-parametric alternatives were used. Regarding multiple testing correction, we applied the Benjamini-Hochberg False Discovery Rate (BH-FDR) procedure. To maintain statistical power while controlling for Type I errors, the corrections were performed within three pre-specified hypothesis families aligned with our research questions: Braak-related comparisons, APOE-related comparisons, and immunofluorescence-based quantitative analyses. Both raw and adjusted P-values have been provided in Supplementary Tables 3, 4, and 5. Statistical significance was set at $*p < 0.05$, $**p < 0.01$, $***p < 0.001$, $****p < 0.0001$.

RESULT

Baseline characteristics of study population

The demographic and neuropathological profiles of the 92 post-mortem human brain cases included in this study are comprehensively summarized in Table 1. Among them, 54 (59 %) were women. Mean age of death was 76.6 (12.2) years. Sixty-four (70%) had the APOE genotype 3/3, and the remainder were APOE4 carriers. To facilitate a granular analysis of pathology progression, the cohort was stratified into four distinct groups based on the hierarchical distribution of NFTs, corresponding to the "B" score of the NIA-AA neuropathologic assessment guidelines. These groups were designated as: B0 (representing Braak stage 0, n=10), B1 (representing Braak stages I or II, n=24), B2 (representing Braak stages III or IV, n=29), and the advanced pathology group B3 (representing Braak stages V or VI, n=29).

Table 1. Baseline characteristic of 92 samples involved in analysis.

	B0, n=10 (Braak stage 0)	B1, n=24 (Braak stage I or II)	B2, n=29 (Braak stage III or IV)	B3, n=29 (Braak stage V or VI)
Age at death (years)	57.1±9.0	72.8±11.8	82.8±7.0	80.4±9.7
Sex, n (%)				
Male	7 (70%)	12 (50%)	13 (45%)	6 (21%)
Female	3 (30%)	12 (50%)	16 (55%)	23 (79%)
PMD (minutes)	351.3±357.0	622±350.9	236.2±342.1	367.3±184.6
APOE, n (%)				
APOE 3/3	10 (100%)	17 (71%)	20 (69%)	17 (59%)
APOE 4 carriers	0 (0%)	7 (29%)	9 (31%)	12 (41%)

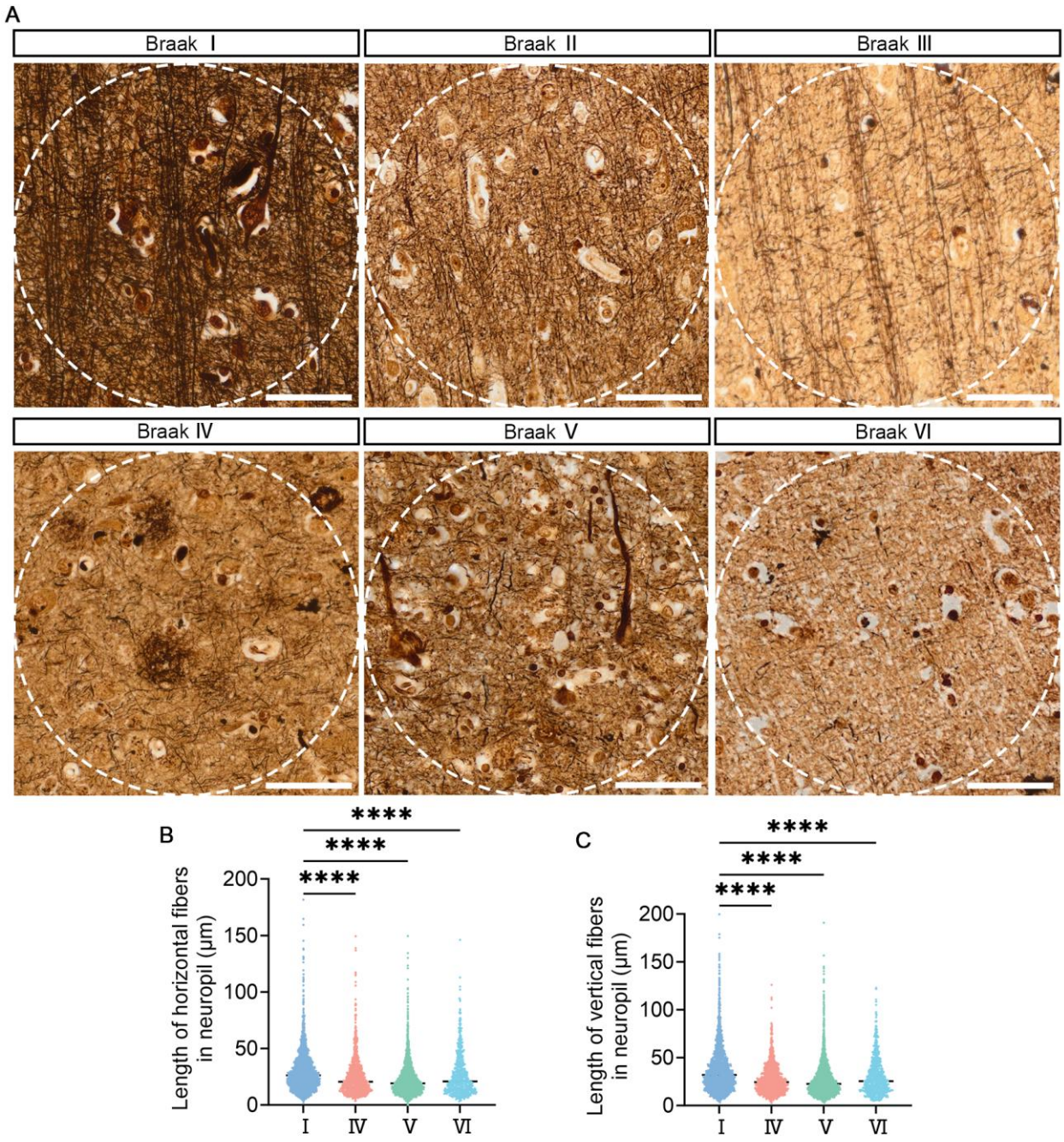

Figure 1. Morphological changes in neuropil fiber length across Braak stages. (A) The neuropil in middle temporal gyrus across samples of different Braak stages, as revealed by Bielschowsky staining. The white dashed circle marks the ROI (200 μm in diameter). Scale bar, 50 μm. **(B–C).** Length of horizontal (**B**) and vertical (**C**) neuropil fibers across different Braak stages. The brain samples from 31 donors were statistically analyzed, including 8 donors at Braak stage I, 6 at Braak stage IV, 12 at Braak stage V, and 5 at Braak stage VI. Each data point represents a single ROI. For this analysis, 60–80 sample slices were evaluated per donor with 2 ROIs per slice; the lengths of 100–200 individual fibers within each ROI were averaged to obtain the final ROI value. Statistical significance was determined using one-way ANOVA. *$p < 0.05$, **$p < 0.01$, ***$p < 0.001$, ****$p < 0.0001$.

Morphological changes of neuropil fiber length

To evaluate the integrity of the neuropil during the progression of AD pathology, this study characterized the morphological changes of the neuropil in cortical layer III of the MTG across Braak stages I– VI. Visual analysis of neuropil degeneration representative Bielschowsky staining images (Fig. 1A) revealed a striking, stage-dependent degradation of the neuropil meshwork. In early Braak stages (I– II), the neuropil fibers appeared dense,

continuous, and well-organized. However, as the Braak stage increased, a progressive intensification of neuropil fiber fragmentation and a gradual thinning of the neuropil density were observed. By the end-stages of the disease (Braak V– VI), the visual evidence showed widespread fiber breakage and severe attenuation; the once-intricate fiber network was largely disintegrated, no longer exhibiting its characteristic organized mesh-like appearance.

Quantitative analysis of the fiber length further substantiated these visual observations. This study measured the lengths of both horizontal and vertical neuropil fibers within a circular ROI 200 μm diameter. The data demonstrated a clear negative correlation between fiber length and disease progression: as the Braak stage advanced, both horizontal and vertical fiber lengths significantly decreased. Notably, the lengths of neuropil fibers in Braak stages IV, V, and VI already exhibited significant reductions compared to those in Braak stage I (Fig. 1B, C). These findings indicate that the shortening and fragmentation of neuropil fibers within the layer III neuropil are closely synchronized with the progression of AD pathology.

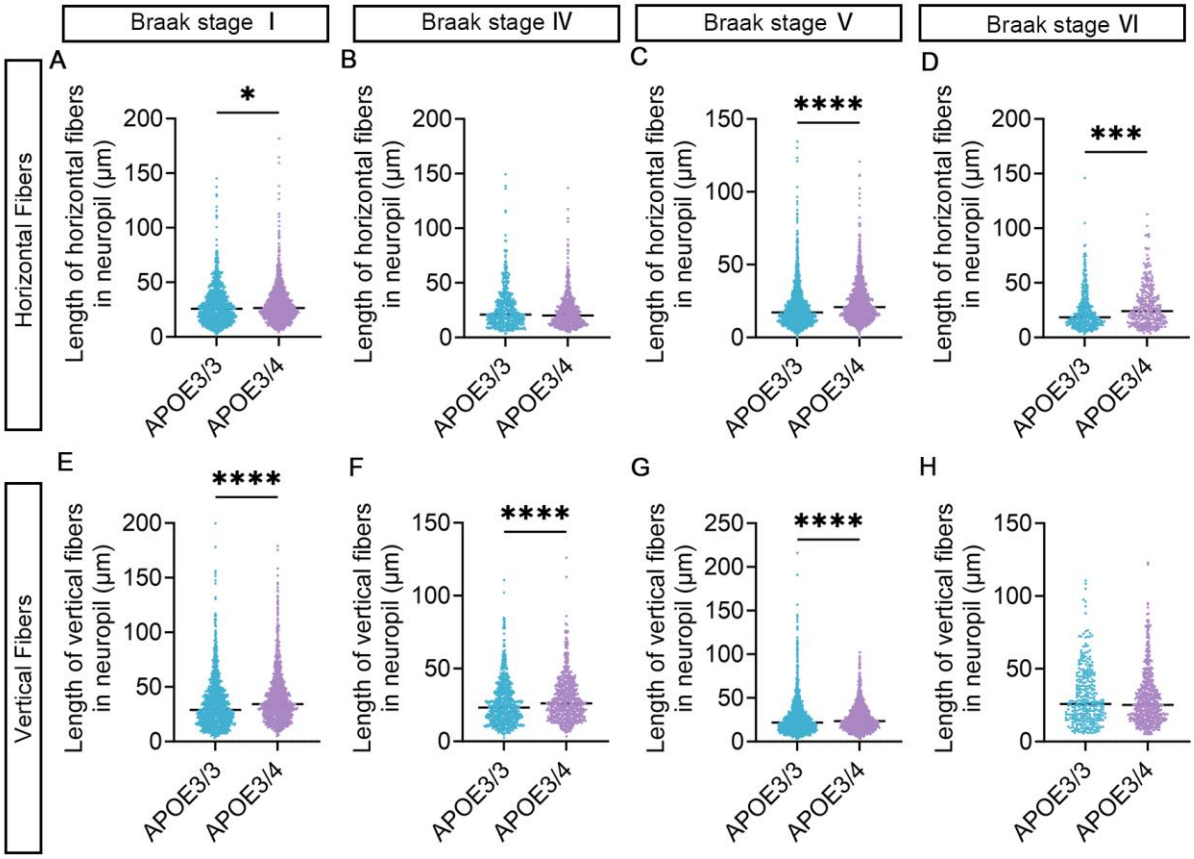

Figure 2. Morphological changes in neuropil fiber length across APOE genotypes. (A-D) Length of horizontal neuropil fibers from Braak Stage I (**A**), Braak Stage IV (**B**), Braak Stage V (**C**), Braak Stage VI (**D**) samples across different APOE genotypes. **(E-H)** Length of vertical neuropil fibers from Braak Stage I (**E**), Braak Stage IV (**F**), Braak Stage V (**G**), Braak Stage VI (**H**) samples across different APOE genotypes. The brain samples from 31 donors were statistically analyzed, including 8 donors at Braak stage I (4 each for APOE3 and APOE4), 6 at Braak stage IV (3 each for APOE3 and APOE4), 12 at Braak stage V (6 each for APOE3 and APOE4), and 5 at Braak stage VI (3 for APOE3 and 2 for APOE4). Each data point represents a single ROI. For this analysis, 60–80 slices were evaluated per donor with 2 ROIs per slice; the lengths of 100–200 individual fibers within each ROI were averaged to obtain the final ROI value. Statistical significance was determined using unpaired *t-tests*. *$p < 0.05$, **$p < 0.01$, ***$p < 0.001$, ****$p < 0.0001$.

To determine whether the genetic risk factor APOE4 differentially modulates neuropil structural integrity, quantitative morphometry of horizontal and vertical neuropil fiber lengths was stratified by APOE genotype (3/3 vs. 4/3) across Braak stages (Fig. 2). In the initial phase of pathology (Braak stage I), APOE4 carriers exhibited significantly greater lengths in both horizontal and vertical neuropil fibers compared to APOE3 homozygotes (Fig. 2A, E). At Braak stage IV, statistically significant differences were no longer observed in horizontal fibers (Fig. 2B), whereas a highly significant divergence persisted in vertical fibers (Fig. 2F). In Braak

stage V, APOE4 carriers again displayed significantly longer horizontal and vertical fibers compared to APOE3 carriers (Fig. 2C, G), this trend persisted into Braak stage VI for horizontal fibers (Fig. 2D), although the distinction in vertical fibers was less pronounced (Fig. 2H). In addition, we analyzed the length of horizontal and vertical fibers in the neuropil from cases at Braak stages II and III (Supplementary Fig. 3). At Braak stage II, the lengths of both horizontal and vertical fibers were significantly greater in the APOE3/4 group compared to the APOE3/3 group (Supplementary Fig. 3A, B). At Braak stage III, a difference between the two genotypes was maintained in the length of horizontal fibers (Supplementary Fig. 3E); however, no significant differences were observed in the length of vertical fibers (Supplementary Fig. 3F).

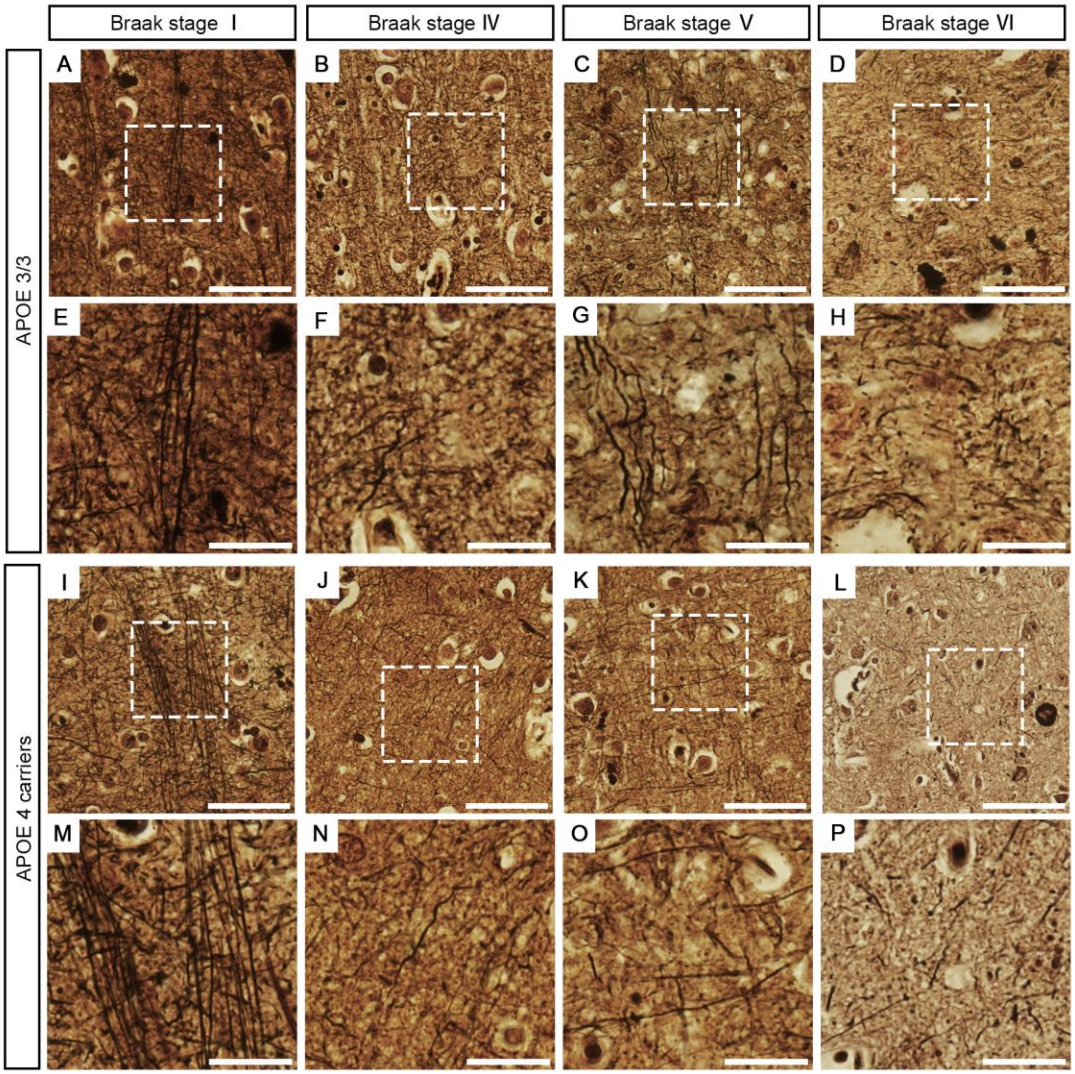

Figure 3. Examples of neuropil fiber curvature across Braak stage and APOE genotype (MTG). Panels below show corresponding magnified views of the regions indicated by white dashed boxes. (**A– D, I– L**) Scale bar, 50 μm. (**E– H, M– P**) Scale bar, 20 μm.

Morphological changes of neuropil fiber curvature

To visually corroborate the quantitative findings regarding fiber deformation, microscopic images of neuropil fibers in the MTG were examined across diverse Braak stages and APOE genotypes, with representative examples presented (Fig. 3). Visual assessment indicated a significant shift in fiber average curvature concomitant with disease progression (Fig. 3A– P). While fibers in Braak stage I largely maintained smooth and linear profiles (Fig. 3A, E, I, M), a distinct loss of this structural linearity was evident in Braak stages IV–VI, characterized by meandering courses and gross disorganization (Fig. 3B–D, F– H, J– L, N– O). Furthermore, at matched Braak stages, the curvature of neuropil fibers in APOE4 carriers appeared visually higher, especially in Braak stages IV and V (Fig. 3B, C, F, G, J, K, N, O).

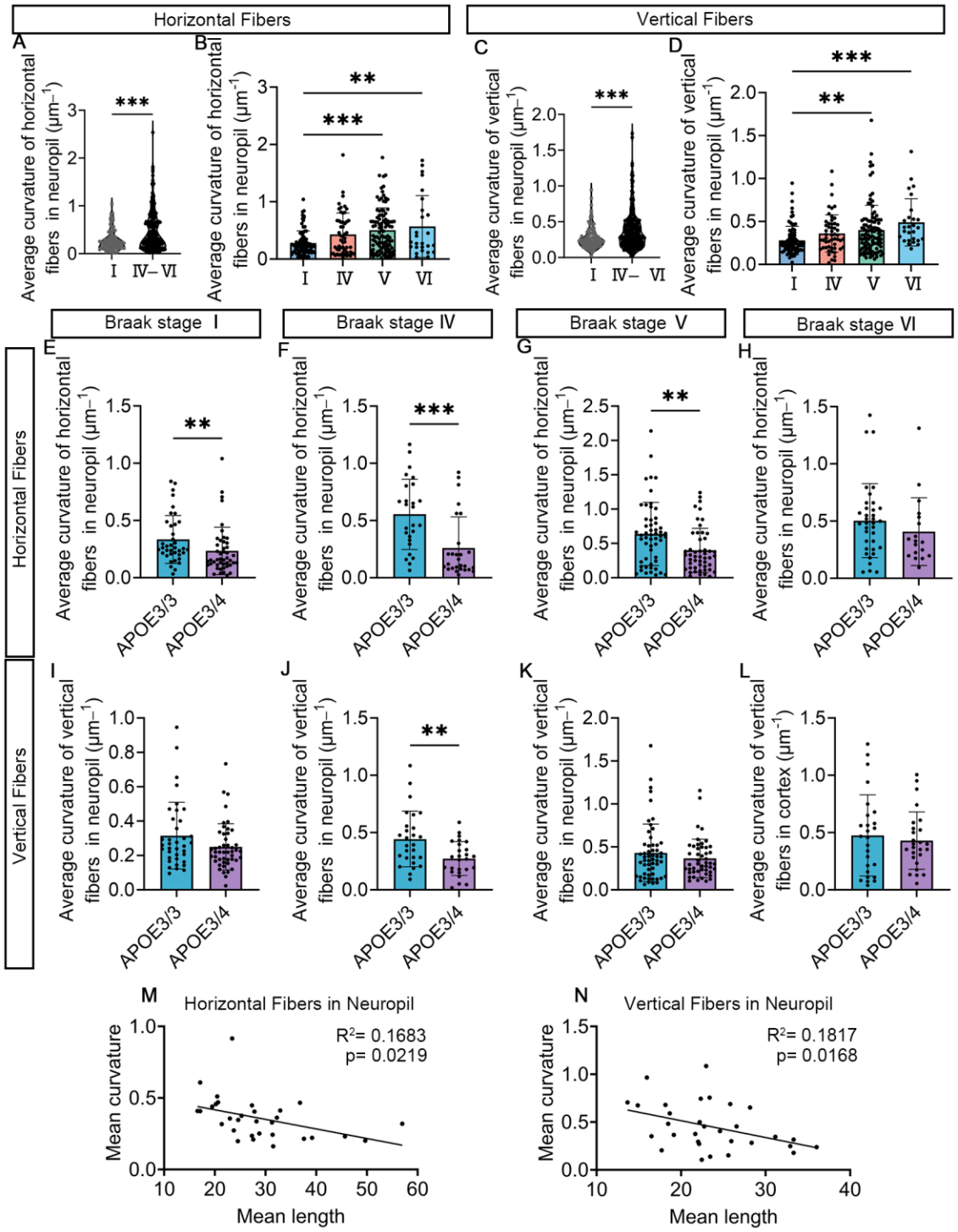

Figure 4. Morphological changes in neuropil fiber average curvature. (A-B) Average curvature of horizontal neuropil fibers across different Braak stages. **C– D.** Average curvature of vertical neuropil fibers across different Braak stages. **E– H.** Average curvature of horizontal neuropil fibers from Braak Stage I (**E**), Braak Stage IV(**F**), Braak Stage V(**G**), Braak Stage VI (**H**) samples across different APOE genotypes. **I– L.** Average curvature of vertical neuropil fibers from Braak Stage I (**I**), Braak Stage IV (**J**), Braak Stage V (**K**), Braak Stage VI (**L**) samples across different APOE genotypes. **M– N.** Scatter plots illustrating the relationship between mean fiber length (x-axis) and mean curvature (y-axis) for horizontal fibers (**M**) and vertical fibers (**N**) within the neuropil. Each data point represents an individual subject.

Quantitative analysis established a distinct association between the advancement of AD pathology and the geometric distortion of neuropil fibers (Fig. 4A–D). Horizontal and vertical neuropil fibers presented an analogous pattern of morphological alteration, wherein the aggregated data for Braak stages IV– VI exhibited significantly higher average curvature compared to Braak stage I (Fig. 4A, C). Subsequent stage-specific stratification confirmed Braak stage V and Braak stage VI manifested markedly elevated average curvature indices relative to the Braak stage I (Fig. 4B, D).

When stratified by APOE genotype, horizontal neuropil fibers demonstrated superior sensitivity to genotypic variations compared to vertical fibers. Across multiple stages of the disease, APOE3 homozygotes consistently exhibited significantly higher average curvature values compared to APOE4 carriers. This distinct morphological profile was evident as early as Braak stage I (Fig. 4E) and persisted through the Braak stage IV (Fig. 4F) into the later Braak stage V (Fig. 4G). While vertical neuropil fibers showed limited sensitivity to APOE genotype, average curvature did not exhibit clear trends at Braak I or Braak V–VI within our current cohort (Fig. 4I, K, L). A variance was only observed in Braak stage IV, where, mirroring the horizontal fibers, APOE3 carriers displayed greater average curvature than APOE4 carriers (Fig. 4J). At Braak stage II, the average curvatures of these fibers were significantly lower in the APOE3/4 group (Supplementary Fig. 3C, D, I). At Braak stage III, no significant differences were observed in the average curvatures of either horizontal or vertical fibers (Supplementary Fig. 3G, H, J).

Linear regression analyses across the entire continuum of Braak stages (I–VI) revealed a progressive shortening of fiber length and a gradual exacerbation of fiber curvature (Supplementary Fig. 3K– N). However, these observations are exploratory and should be interpreted with caution, given the limited sample size and statistical power for the intermediate stages (Braak II and III). Bearing this limitation in mind, these continuous trends suggest that the morphological degeneration of neuropil fibers may undergo a gradual process throughout disease progression.

To investigate the relationship between the geometric properties of neuropil fibers, the correlation between the morphometric parameters of fiber length and curvature was analyzed across all study samples. (Fig. 4M, N). Scatter plot analysis revealed a distinct negative correlation between these two morphometric parameters. Samples characterized by shorter mean fiber lengths consistently exhibited higher mean curvature values. This trend indicates that as neuropil fibers shorten, they simultaneously exhibit increased tortuosity. This negative correlation was evident in both the horizontal (Fig. 4M) and vertical (Fig. 4N) fiber populations. Preliminary correlation analyses between fiber length and curvature were also conducted across Braak stages and genotypes (Supplementary Fig. 5A– L). Although all of them consistently exhibited a negative correlational trend, owing to the limited sample size available for high-resolution tracing, these trends did not reach statistical significance and should be interpreted as exploratory.

The coordinates for each point were derived by calculating the arithmetic mean of the length and curvature of neuropil fibers identified within the ROI for that sample. The brain samples from 31 donors were statistically analyzed, including 8 donors at Braak stage I (4 each for APOE3 and APOE4), 6 at Braak stage IV (3 each for APOE3 and APOE4), 12 at Braak stage V (6 each for APOE3 and APOE4), and 5 at Braak stage VI (3 for APOE3 and 2 for APOE4). Each data point represents a single ROI. For this morphological analysis, 5–6 slices were evaluated per donor with 2 ROIs per slice; the curvatures of 3–6 individual fibers within each ROI were averaged to obtain the final ROI value. Statistical significance was determined using one-way ANOVA for A– D, and unpaired *t-tests* for E– L. $*p < 0.05$, $**p < 0.01$, $***p < 0.001$, $****p < 0.0001$.

Evaluation of Microstructural Components of the Neuropil

To verify whether the structural deformations observed previously correspond to alterations in protein expression, quantitative analysis of MBP and AT8 mean fluorescence intensity (MFI) was performed in the MTG, stratified by APOE genotype and Braak stage (Fig. 5). Morphological examination revealed a progressive deterioration of neuropil architecture correlating with advancing disease stages. In the early stage (Braak I), neuropil maintained a linear, continuous structure with organized myelination in both APOE3 and APOE4 carriers. However, as pathology progressed to late stages (Braak V and VI), a profound disruption of fiber integrity was observed (Fig. 5A). Quantitative analysis of MBP immunoreactivity demonstrated that genotype-driven discrepancies are most detectable during the transitional phase of the disease. In Braak stage I, myelin density appeared comparable between the investigated genotypes (Fig. 5B). Notably, in Braak stage IV, APOE4 carriers exhibited a highly significant elevation in MBP fluorescence intensity compared to APOE3 homozygotes (Fig. 5C). A similar pattern was observed in tau pathology. While AT8 levels were comparable between genotypes in Braak stage I (Fig. 5F), APOE4 carriers displayed a marked surge in phosphorylated tau burden during Braak stage IV (Fig. 5G), this aligns with established evidence that APOE4 exacerbates tau-mediated neurodegeneration. In Braak V

and VI, the severe morphological alterations observed qualitatively in Fig. 5A appeared to impact quantitative resolution. Despite the documented progression of the disease, MBP fluorescence intensity did not manifest clear genotype-driven divergence at Braak V (Fig. 5D) or Braak VI (Fig. 5E) within the constraints of our current limited sample size. Similarly, distinct AT8 stratification between genotypes became less discernible at Braak V (Fig. 5H), with an observational trend of slight AT8 elevation in APOE4 cases at Braak VI (Fig. 5I). In addition, immunofluorescence data of AT8 and MBP for Braak stages II and III were also presented in Supplementary Fig. 4A– E.

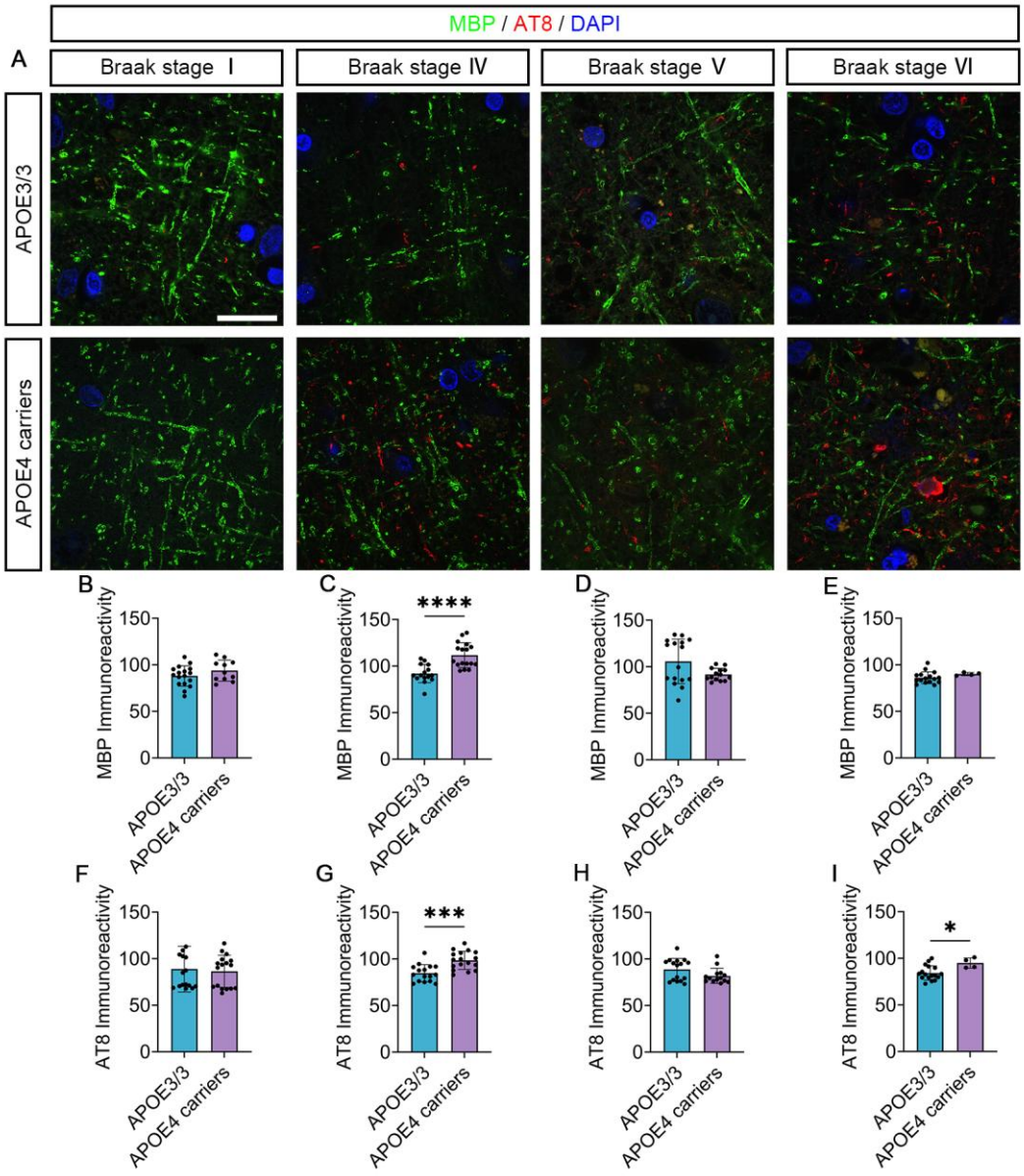

Figure 5. Quantification of MBP and AT8 levels in APOE3 and APOE4 carriers stratified by Braak stage. (A) Representative double-label immunofluorescence images showing MBP and AT8 expression. Scale bar, 20 μm. **(B-E)** Quantitative analysis of MBP MFI across APOE genotypes at Braak stage I (**B**), IV (**C**), V (**D**), and VI (**E**). **(F-I)** Quantitative analysis of AT8 MFI across APOE genotypes at Braak stage I (**F**), IV (**G**), V (**H**), and VI (**I**). The brain samples from 16 donors were statistically analyzed, including 5 donors at Braak stage I (2 for APOE3 and 3 for APOE4), 4 at Braak stage IV (2 each for APOE3 and APOE4), 4 at Braak stage V (2 each for APOE3 and APOE4), and 3 at Braak stage VI (2 for APOE3 and 1 for APOE4). Each data point represents a single ROI. One ROI was selected from each slice, with three to six slices analyzed per donor. Statistical significance was determined using unpaired *t-tests*. *$p < 0.05$, **$p < 0.01$, ***$p < 0.001$, ****$p < 0.0001$.

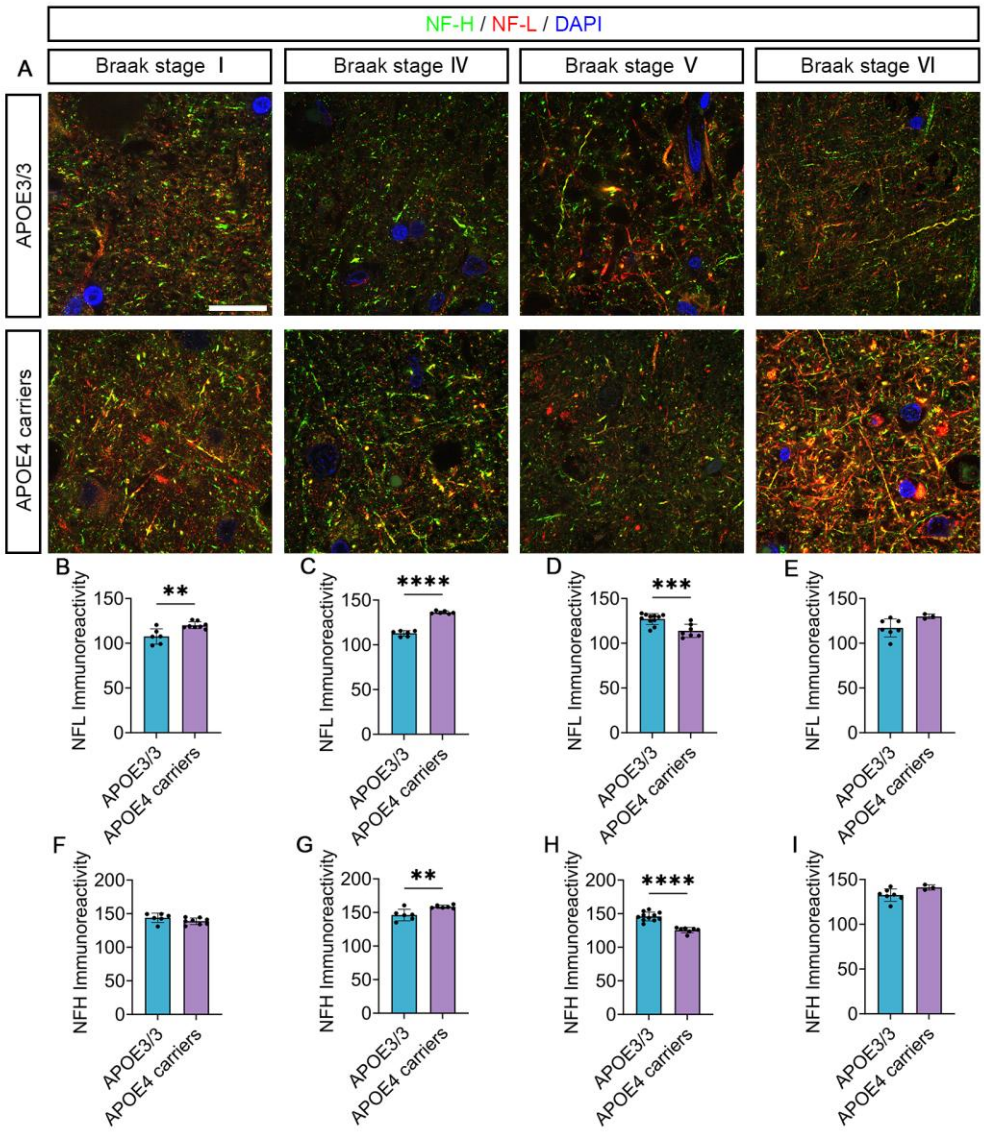

Figure 6. Quantification of NF-L and NF-H levels in APOE3 and APOE4 carriers stratified by Braak stage. **(A)** Representative double-label immunofluorescence images showing NF-L and NF-H expression. Scale bar, 20 µm. **(B-E)** Quantitative analysis of NF-L MFI across APOE genotypes at Braak stage I (**B**), IV (**C**), V (**D**), and VI (**E**). **(F-I)** Quantitative analysis of NF-H MFI across APOE genotypes at Braak stage I (**F**), IV (**G**), V (**H**), and VI (**I**). The brain samples from 16 donors were statistically analyzed, including 5 donors at Braak stage I (2 for APOE3 and 3 for APOE4), 4 at Braak stage IV (2 each for APOE3 and APOE4), 4 at Braak stage V (2 each for APOE3 and APOE4), and 3 at Braak stage VI (2 for APOE3 and 1 for APOE4). Each data point represents a single ROI. One ROI was selected from each slice, with three to six slices analyzed per donor. Statistical significance was determined using unpaired *t-tests*. *$p < 0.05$, **$p < 0.01$, ***$p < 0.001$, ****$p < 0.0001$.

To evaluate cytoskeletal integrity and neuropil damage, quantitative analysis of NF-L and NF-H MFI was assessed in APOE3 and APOE4 carriers across distinctive Braak stages (Fig. 6A). Confocal microscopy revealed that cytoskeletal proteins undergo progressive disorganization. In early stages (Braak I), neuropil displayed continuous, linear morphologies. However, in advanced stages (Braak V-VI), the staining patterns for both NF-L and NF-H became increasingly fragmented and punctate, indicating a breakdown of neuropil continuity (Fig. 6A). Quantitative analysis of NF-L revealed a significant genotype-dependent fluctuation. In the initial phase (Braak I), APOE4 carriers showed a trend of elevated NF-L levels compared to APOE3 homozygotes (Fig. 6B). This accumulation displayed a pronounced increase in Braak stage IV (Fig. 6C), suggesting a potential impairment in neurite transport or clearance mechanisms during the transitional disease phase. However, this trend appeared to shift in Braak stage V, where APOE4 carriers presented with lower

average NF-L intensity than the APOE3 group (Fig. 6D). By Braak stage VI, NF-L levels did not display clear genotype-driven divergence restricted by our current limited sample size (Fig. 6E). A similar, albeit temporally distinct, pattern was observed for NF-H. While baseline levels in Braak stage I were comparable between genotypes (Fig. 6F), a transient surge in NF-H intensity was detected in APOE4 carriers at Braak stage IV (Fig. 6G). Consistent with the NF-L data, Braak stage V suggested a shift in trajectory where APOE4 carriers presented with reduced NF-H fluorescence intensity (Fig. 6H), followed by a lack of distinct observable variation in the terminal Braak stage VI (Fig. 6I). Collectively, these data suggest that neurofilament expression does not follow a linear trajectory but rather exhibits a complex, stage-dependent instability in APOE4 carriers. The apparent shift from accumulation (Stage IV) to reduction (Stage V) highlights high inter-individual heterogeneity and suggests that cytoskeletal protein levels are highly volatile during the rapid progression of neurodegeneration. In addition, immunofluorescence data of NF-H and NF-L for Braak stages II and III were also presented in Supplementary Fig. 4F– J. It is important to note that these APOE subgroup comparisons, particularly at advanced disease stages, involve very small sample sizes. Therefore, while these morphological and immunofluorescence differences are biologically interesting, they should be viewed as preliminary observations and cannot be conclusively interpreted as robust genotype effects.

Staging of neuropil disruption degree

Building upon the trends of neuropil fiber fragmentation within the neuropil revealed by the preceding statistical analyses, a novel grading system was developed to categorize the severity of neuropil structural disruption. This classification, based on Bielschowsky silver staining, defines four distinct stages of tissue integrity ranging from preservation to total fragmentation (Table 2). To ensure clinical and pathological relevance, the assessment window was geometrically constrained to a circular ROI with a 200 μm diameter.

Table 2. Scoring of bielschowsky stained neuropil, that is, Neuropil Disruption Stage.

-	Homogeneous and compact neuropil
+	Neuropil with initial disruption
++	Neuropil with extensive disruption
+++	Complete fragmentation of neuropil fibers and absence of neuropil

In the baseline state, designated as Stage (-) (Fig. 7A), the tissue exhibited a homogeneous and compact neuropil matrix. High-magnification microscopy demonstrated a dense, uninterrupted network of neuropil. The silver impregnation revealed long, continuous fascicles traversing the visual field without evidence of rarefaction or structural discontinuity. The onset of pathological alteration, classified as Stage (+) (Fig. 7B), was characterized by initial disruption of the neuropil meshwork. While the global architecture remained discernible, subtle focal rarefaction was observed. The silver-stained fibers displayed early signs of loosening, with a reduction in the density of fine, interlacing processes compared to the compact state of Stage (-). Progression to Stage (++) (Fig. 7C) was marked by extensive disruption and a conspicuous loss of fiber coherence. The neuropil exhibited significant disorganization, characterized by the breakage of long-range neuritic fibers, the staining pattern appeared fragmented. The most severe stage, Stage (+++) (Fig. 7D), manifested as complete fragmentation of neuropil fibers and an absence of neuropil. In these sections, the characteristic reticular texture was virtually obliterated. The visual field was devoid of continuous neuropil structures, replaced instead by granular argentophilic debris and isolated, truncated neuropil fibers remnants.

Analysis of adjacent sections stained for Phospho-Tau (P-tau) revealed a striking, stepwise association between the severity of structural disruption and the intensity of pathological tau deposition. In samples classified as Stage (-), P-tau immunoreactivity was notably absent, confirming that structural integrity is maintained in the absence of tau pathology (Fig. 7E). Notably, in Stage (+) samples, where silver staining already confirmed initial structural breakdown, P-tau signals remained negligible and lacked distinct positive aggregates (Fig. 7F). This observation suggests that the argyrophilic alteration of the neuropil architecture may antecede the formation of overt P-tau inclusions detectable by standard immunohistochemistry. As structural damage advanced to Stage (++), P-tau signals became pronounced and clearly defined (Fig. 7G). Finally, in the most severe Stage (+++) cases, P-tau staining appeared as highly dense, intensely pigmented aggregates (Fig. 7H).

To demonstrate the reproducibility and robustness of this staging system, two representative images natively derived from two independent patient cases are presented

side-by-side for each specific grade within every distinct brain region (Supplementary Fig. 6, 7). Morphological consistency within grades validates that the criteria are robust to individual heterogeneity.

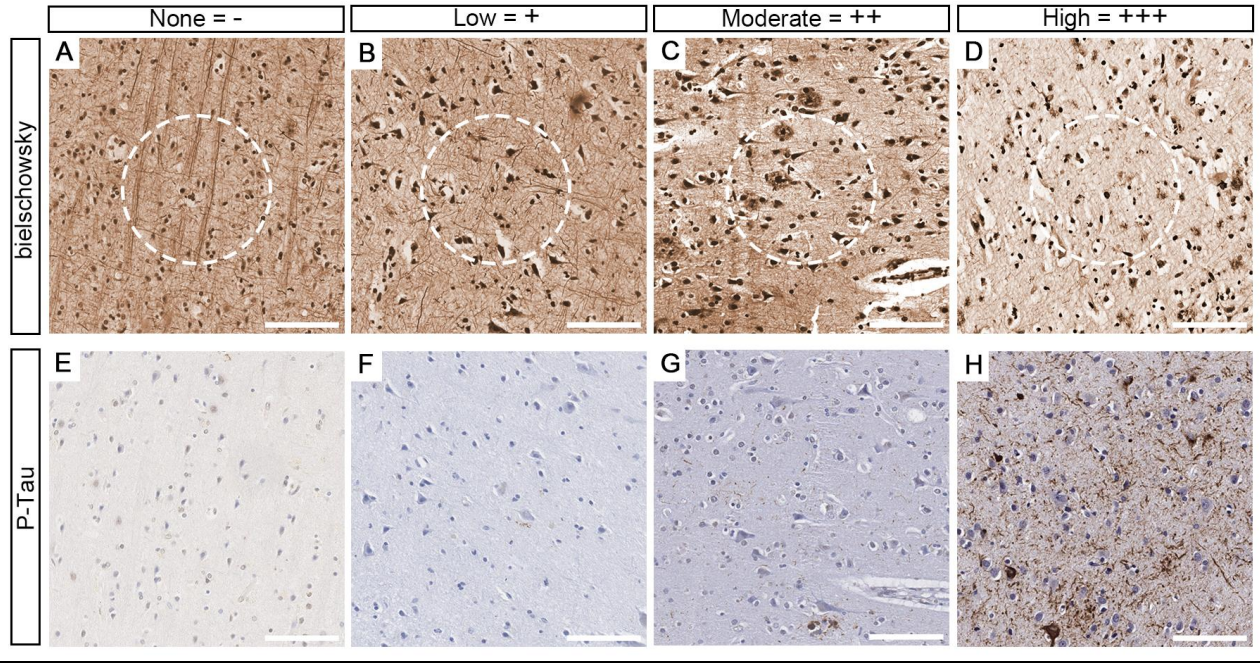

Figure 7. Bielschowsky and P-tau staining of neuropil with differing stages of disruption. (A-D) Bielschowsky staining illustrating the progression of degeneration: (**A**) None (-), homogeneous and compact neuropil; (**B**) Low (+), initial disruption; (**C**) Moderate (++), extensive disruption; and (**D**) High (+++), complete fiber fragmentation and neuropil loss. **(E-H)** Corresponding P-tau immunostaining in adjacent sections matched to the Bielschowsky staining. All sections were taken from temporal lobe. Scale bar, 100 μm.

Spatiotemporal Patterns of Neuropil Disruption across Pathological Staging

Based on the aforementioned staging system for neuropil disruption, cortical layer III was evaluated and graded across eight distinct brain regions: EC, Amy, aHipp, bHipp, MTG, MFG, IPL, and OCC. To systematically validate the pathological relevance of the established neuropil grading system, the distribution of disruption scores (ranging from None to High) was mapped against the canonical "ABC" neuropathological criteria: Thal amyloid phase (Fig. 8A), Braak NFT stage (Fig. 8B), and CERAD plaque score (Fig. 8C). The blue line indicates the progression of pathology across brain regions, using the ordering defined by the staging system applied in each panel. The association between neuropil integrity and the canonical hierarchies of AD pathology was systematically mapped across distinct brain regions. The distribution of neuropil disruption scores, ranging from None (-) to High (+++), was visualized using color-coded heat maps, revealing disparate spatial trajectories relative to Aβ versus tau pathology.

When brain regions were stratified according to the Braak NFT stages, the pattern of neuropil disruption demonstrated a strong spatiotemporal concordance with the hierarchical spread of tau pathology. As indicated by the pathological progression trajectory (blue line), severe neuropil fragmentation (Stage +++ and ++) was initially clustered in medial temporal limbic structures, including the EC and Amy. As the Braak stages advanced (V– VI), high-stage disruption progressively extended into isocortical regions such as the MTG and OCC (Fig. 8B). A similar trend was observed in the analysis based on CERAD plaque scores (Fig. 8C). The severity of neuropil degeneration closely paralleled the density of neuritic plaques, with the heat map exhibiting a diagonal gradient of increasing disruption intensity that matched the ascending CERAD categories. This suggests that neuropil architectural loss is tightly coupled with the accumulation of neuritic and neurofibrillary lesions.

In contrast, the spatial distribution of neuropil disruption exhibited a marked divergence from the progression pattern of Aβ deposition defined by Thal phases (Fig. 8A). While Thal staging typically initiates in neocortical areas, the heat map revealed that regions with early and high amyloid load (e.g., OCC, MFG in Thal phases 1– 3) frequently displayed preserved neuropil structure (predominantly Stage - or +). Conversely, regions notoriously susceptible to early structural damage, such as the aHipp, bHipp and EC, exhibited

severe disruption (Stage +++), even in cases where the global amyloid phase was not yet terminal.

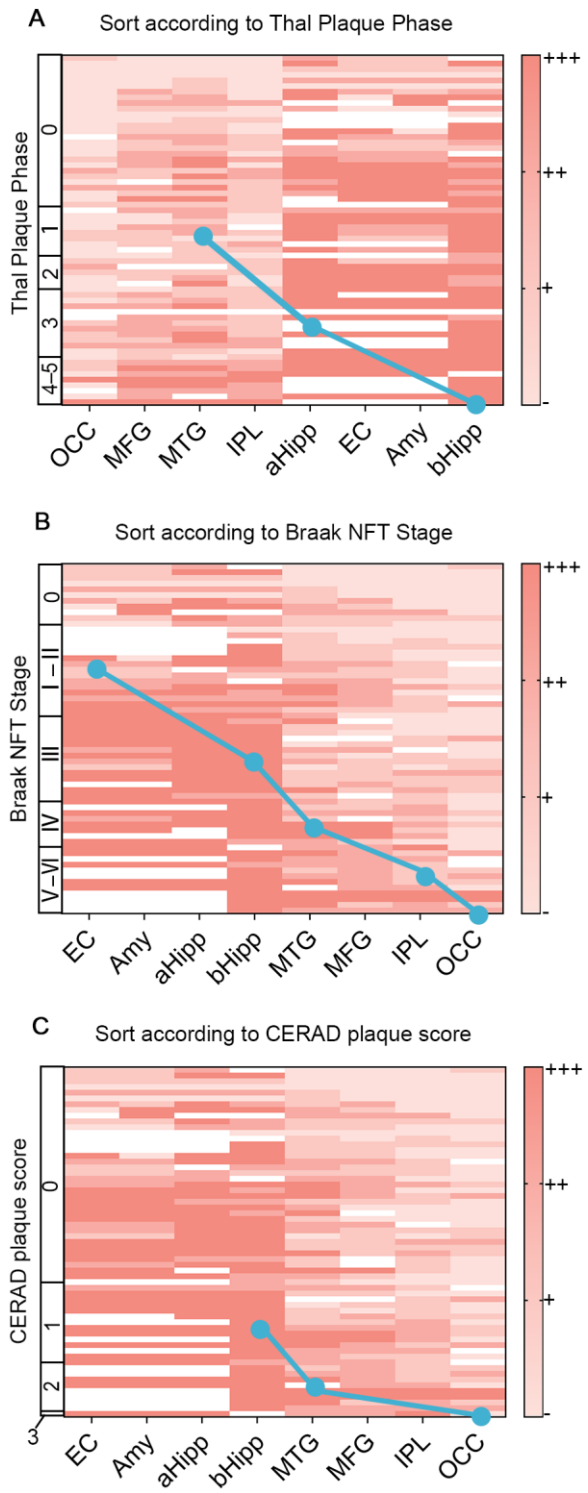

Figure 8. Heat maps of neuropil disruption and pathology progression across brain regions based on Thal, Braak, and CERAD staging. The level of neuropil disruption is scored on a four-stage scale: None (-), Low (+), Moderate (++), High (+++), the colour-coding scheme was used to represent the neuropil pathology stage in the heat maps. **A.** Brain regions sorted according to Thal plaque phase. **B.** Brain regions sort according to Braak NFT Stage. **C.** Brain regions sort according to CERAD plaque score. The boxes coloured in white in the heat maps indicate missing data. The blue line indicates the progression of pathology across brain regions, using the ordering defined by the staging system applied in each panel. The brain samples from 61 donors were statistically analyzed, including 10 samples at Braak stage 0, 6 samples at Braak stage I, 10 samples at Braak stage II, 15 samples at Braak stage III, 8 at Braak stage IV, 5 at Braak stage V, and 7 at Braak stage VI.

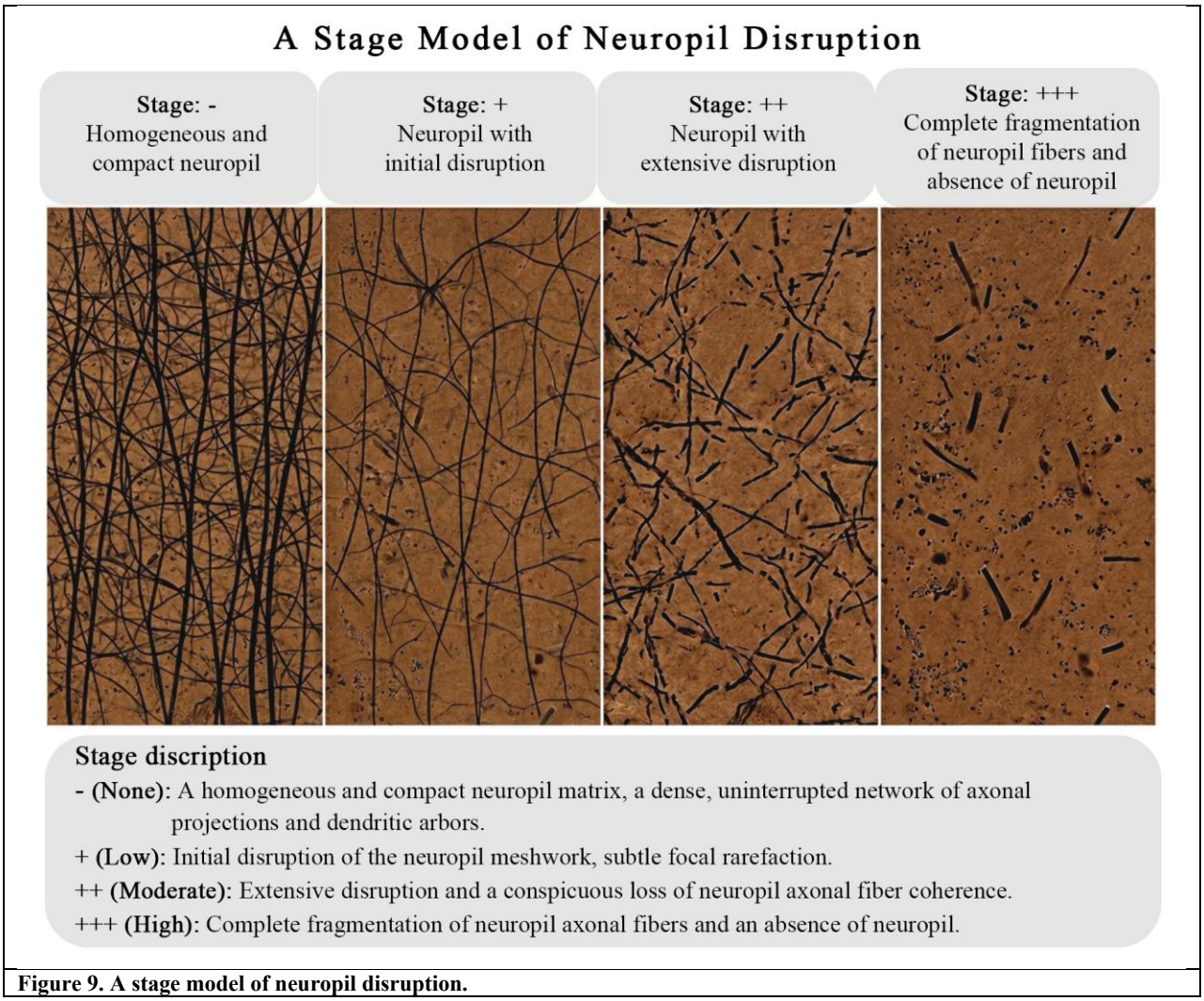

Figure 9. A stage model of neuropil disruption.

To contextualize these findings, a visual model illustrating the sequential progression of neuropil disruption is proposed (Fig. 9).

DISCUSSION

The findings presented in this study provide a granular morphometric analysis of neuropil within the MTG by quantifying fiber length and curvature in Bielschowsky-stained cortical layer III, thereby characterizing the progressive erosion of the neuropil fibers architecture. The principle of Bielschowsky staining relies on the argyrophilia of neurofibrils (i.e., the axonal cytoskeleton, neurofilaments and microtubules) [21, 22]. To ensure the specificity of neuropil quantification within the Bielschowsky-stained sections, we implemented strict morphological criteria to distinguish neuritic fiber profiles from other argyrophilic elements. While Bielschowsky silver staining labels a broad spectrum of neurofibrillary structures, its high contrast and resolution allow for reliable morphological differentiation based on established neuroanatomical hallmarks. Specifically, axons were identified by their slender, uniform diameter and long-range, non-tapering trajectories [23]. In contrast, dendritic profiles, characterized by significant tapering toward the cell body and more frequent, acute-angle branching, were systematically excluded from the analysis [24]. Furthermore, NFTs and NT were readily distinguished and omitted due to their distinct flame-shaped or highly convoluted, irregular morphologies [16]. In the context of AD pathology, this technique specifically visualizes pathological neuritic structures, including dystrophic neurites around plaques, NT and NFTs [25]. Consequently, the observed phenomena under this method, such as fragmentation, swelling, abnormal curvature, and rarefaction of neuropil, are morphological representations of axonal transport deficits, cytoskeletal collapse, and ultimate degeneration in the AD pathological cascade [13, 26-28]. This provides a reliable technical foundation for systematically quantifying the

geometric degradation patterns of neuropil within the Braak staging framework.

While the term "neuropil" broadly encompasses a dense matrix of axons, dendrites, and glial processes, the argentophilic fibers quantified in cortical Layer III, the principal source of cortico-cortical association projections, predominantly represent axonal fascicles [29]. This study focuses on the neuropil fibers in layer III of the cerebral cortex. Association fibers are pathways that connect cortical areas within the same cerebral hemisphere and are formed primarily by the axons of neurons located in cortical layers II and III [30, 31]. Cells in layer III preferentially provide the long association fibers, including commissural fibers [29], these long association fibers form compact bundles that traverse deeper white matter and connect different lobes within the same hemisphere [32]. As the bundles tracts that interconnect distant cortical regions, long association fibers exhibit substantial disturbances of the structural connectivity as early as the initial stages of AD [33, 34]. Consequently, these fibers' length and curvature serve as primary morphometric parameters to characterize the pathological status of the cortical neuropil.

Analysis of length and curvature of neuropil fibers by Braak stages

The results demonstrate a stage-dependent continuum of structural failure: as Braak staging advances, these neuropil fibers undergo significant shortening and geometric distortion (increased curvature). Within the dense meshwork of the neuropil, the axon constitutes the primary structural element responsible for long-range communication, and its continuity is paramount for network function. One of neurodegenerative process in AD is characterized by retrograde degeneration of the axons [35, 36], and the concept of "dying-back" axonopathy, a foundational principle in neurodegeneration, posits that pathological insults often manifest first as distal axonal degeneration, a process that physically shortens the neuron's reach long before somatic death [37]. This structural failure is mechanistically linked to the breakdown of the axonal cytoskeleton, particularly the microtubule network responsible for maintaining axonal length and facilitating transport [38]. Therefore, the measurement of a continuous neuropil fiber segment's length is, in essence, a direct quantification of the physical continuity of the underlying axonal cytoskeleton, any reduction in this length is indicative of fragmentation, a terminal event in the process of axonal degeneration. The significant, stage-dependent reduction in horizontal and vertical fiber length observed in this study directly corroborates these foundational principles and aligns with neuropathological consensus. Specifically, analyses of both horizontal and vertical fibers consistently demonstrate a statistically significant reduction in length beginning at Braak stage IV when compared to the early-stage (Braak I) baseline, a trend that persists and exacerbates into later stages (V and VI). While prior research has inferred this degenerative process, its focus has often been constrained to mechanistic investigations of specific axonal compartments (e.g., the axon initial segment) or the quantification of functionally-related structures such as dendritic spines and synaptic terminals [39, 40], thus offering predominantly indirect or mechanistic evidence for the overarching phenomenon of global axonal retraction. The present study, therefore, provides direct, micrometer-scale quantitative corroboration for the progressive disintegration of the cortical neuropil in AD. In essence, while Braak staging charts the topographical spread of tau pathology, these morphometric data translate this pathological progression into a precise measure of its physical consequence: the catastrophic failure of neuropil integrity.

Parallel to the loss of fiber length, this study identified a significant increase in fiber curvature in the advanced stages of AD (Braak V-VI). This morphological transformation, characterized by a transition from linear to meandering and disorganized trajectories in the MTG, suggests that geometric distortion is a hallmark of late-stage AD pathology. The quantitative escalation of curvature indices in Braak stages V and VI is not merely a geometric anomaly but provides a macroscopic window into the molecular disintegration of the neuronal cytoskeleton. It is widely accepted in neuroscience that "fiber curvature" reflects cytoskeletal stability, specifically the integrity of the microtubules (MTs) lattice. The morphology and physiology of neuropil crucially depend on the parallel bundles of MTs, running all along to serve as their structural backbones and highways for life-sustaining cargo transport and organelle dynamics [41]. However, in the context of AD, the pathological hyperphosphorylation of tau protein disrupts this stability, pathological tau causes microtubule disassembly and the impairment of axonal transport, which leads to the loss of structural rigidity and subsequent morphological buckling [42]. This sequence of molecular events supports the interpretation that the observed increase in fiber curvature is a direct downstream consequence of the cytoskeletal collapse inherent to tauopathies. The finding that fiber curvature exacerbates specifically with advancing Braak stages is entirely consistent with existing neuropathological literature. The Braak staging system itself is predicated on the stereotypical spread of NFTs, which are aggregates of filamentous tau, the correlation between Braak stage progression and increased fiber curvature reported herein

provides a quantitative morphological bridge between molecular tau pathology and gross tissue degeneration.

Analysis of length and curvature of neuropil fibers by APOE genotype

By employing quantitative morphometry across varying Braak stages, our study reveals a distinct pathological trajectory: APOE4 carriers exhibited significantly preserved neuropil fiber lengths compared to APOE3 homozygotes in both incipient (Braak I) and terminal (Braak V– VI) phases, yet this distinction notably vanished during the critical limbic-to-neocortical transition (Braak IV). Furthermore, we observed a genotype-dependent divergence in fiber geometry, characterized by consistently higher curvature in APOE3 carriers and a more linear straightness observed in APOE4 carriers. This genotype-dependent divergence was most pronounced in horizontal fibers, which correspond to long-range intracortical association tracts. Consistent with the well-established selective vulnerability of these circuits in AD, horizontal fibers exhibited superior sensitivity to genotypic variations compared to the more resilient vertical projection fibers [43, 44], suggesting that horizontal connections are more sensitive indicators of APOE-mediated structural alterations than vertical projection fibers. Additionally, our findings indicate that while these morphological distinctions are prominent during the early-to-intermediate stages of the disease, they are ultimately obliterated by the saturation of pathology as neurodegeneration becomes widespread in the terminal stages.

Rather than interpreting the observed preservation of fiber length strictly as neuroprotection, we propose the hypothesis that these retained long-range fibers in APOE4 carriers may paradoxically facilitate disease progression. Pioneering studies have confirmed that neurodegenerative diseases are not merely a diffuse injury, but a network-based disease that progresses along neuroanatomical connections [45], some authors have suggested that neurodegeneration may relate to neural network dysfunction [46, 47]. And the pathological progression of Tau protein does not follow physical proximity but proceeds strictly along anatomical connectivity pathways, propagating trans-synaptically in a prion-like manner [47, 48]. In this context, we propose a hypothetical mechanism wherein the preserved longer fibers observed in APOE4 carriers may potentially constitute a more efficient structural substrate, serving as a putative anatomical “highway”, for the inter-regional propagation of pathological proteins. This hypothesis is supported by evidence that axonal microtubule stability is critical for long-distance axonal transport, simultaneously providing the necessary tracks for pathological Tau projections from the entorhinal cortex to the hippocampus and subsequently to the neocortex [11, 49]. Consequently, we speculate that an intact axonal cytoskeleton could inadvertently lower the resistance for pathological diffusion. This structural facilitation likely operates in conjunction with APOE4-mediated metabolic deficits. Since APOE4 is forms significantly reduce cerebral Aβ clearance rates and may promote Tau phosphorylation and aggregation by influencing lipid metabolism [50-52], and microglial dysfunction and blood-brain barrier leakage induced by APOE4 prevent the effective degradation of toxic proteins in the extracellular environment [53-55], the presence of the longer axons may potentially provide convenient channels for these uncleared toxic proteins to diffuse throughout the brain. This may lead to a rapid rise in pathological protein concentration at synaptic terminals, potentially triggering more severe synaptic loss and cognitive decline. This aligns with observations that synaptic damage, which correlates strongly with cognitive decline [56, 57], may be accelerated by efficient network-based transmission [58]. Regarding the divergence in curvature, we speculate a hypothetical mechanism in which the higher curvature in APOE3 carriers might represents a compensatory response, where neurons retain the capacity to reorganize their cytoskeleton under stress, such as via microtubule polymerization [59].In contrast, the straightness observed in APOE4 carriers may indicate an impaired plasticity phenotype. This concept resonates with recent findings in glial biology, it was demonstrated that APOE4 imparts an impaired response phenotype, where cells fail to transition into a disease-associated reactive state under stress, effectively becoming locked in a homeostatic but maladaptive quiescence [60]. Drawing a speculative parallel to neuronal cytoarchitecture, APOE4 carriers may similarly lack the capacity for the tortuous growth associated with attempts at repair. This makes sense given established in vitro evidence APOE4 actively inhibits neurite outgrowth and branching compared to APOE3 [59, 61]. Consequently, the linear morphology in APOE4 samples might not represent health, but rather a potentially stunted or fragmented architecture.

Correlation between neuropil fiber length and curvature

Our morphometric analysis revealed a significant negative correlation between fiber length and curvature: as neuropil fibers shorten, they exhibit progressively higher curvature indices. This statistical relationship is crucial for interpreting the pathological landscape of AD, as it suggests that fiber fragmentation and morphological deformation are not independent events but rather concurrent manifestations of the same degenerative

process. While "curvature" is a mathematical index of tortuosity, histologically, the high-curvature segments observed in AD samples correspond to specific pathological alterations. While significant ($p<0.05$), the low R^2 values (0.16–0.18) reflect a limited effect size, suggesting that fiber length may not the sole determinant of curvature.

The negative correlation implies that degenerating axons transition through morphological distortion, not abrupt loss, this aligns with the established degenerative sequence of beading or focal swelling [62-64]. During this process, the shortening of axonal fiber bundles reflects underlying microtubule disassembly and axonal atrophy [63]. This loss of structural integrity diminishes internal tension, allowing membrane tension to drive a shape instability [62], therefore the axon transitions from a linear cylinder into a series of high curvature undulations or beads [64], directly linking overall tract shortening to a quantifiable increase in local curvature index. Consequently, the concomitant reduction in length and increase in curvature constitute a distinct morphological signature of the AD neuropil, reflecting a unified state of cytoskeletal collapse where the loss of connectivity is physically inseparable from geometric destabilization.

A novel staging system for neuropil disruption

Based on the above conclusions regarding the degeneration of neuropil fibers, this study provides a quantitative framework to characterize the progressive breakdown of axonal-dendritic networks in AD. This staging system, based on Bielschowsky silver staining, captures distinct morphological transitions from compact, homogeneous neuropil (Stage -) to complete fiber fragmentation and loss of reticular texture (Stage +++). Notably, the stepwise correlation between increasing neuropil disruption and P-tau burden further reinforces the interdependence of cytoskeletal damage and tau pathology. Immunohistochemical validation clarified the molecular mechanisms underpinning these morphological alterations: the observed shortening and buckling of silver-stained fibers coincided with stage-dependent fluctuations in NF-L and NF-H, alongside a progressive loss of MBP. These findings confirm that our histological grading reflects intrinsic cytoskeletal disassembly and demyelination. Crucially, the spatial distribution of these structural defects strongly correlated with P-tau (AT8) accumulation. This stepwise association reinforces the concept that axonal transport deficits and cytoskeletal breakdown are inextricably linked to tau pathology [49]. This aligns with studies showing that neurofilament fragmentation and microtubule destabilization accelerate tau hyperphosphorylation and NFT formation, ultimately driving neuritic dystrophy and synaptic loss [65, 66].

While the progression of neuropil disruption spatially overlaps with the established spread of Tau (Braak) and neuritic plaque (CERAD) pathologies, it follows a negative anatomical trajectory to that of expansive amyloid deposition (Thal). This dissociation indicates that neuropil disintegration is morphologically distinct from diffuse amyloidosis and is more directly dependent on the cytoskeletal pathology characteristic of tauopathy. The observed divergence between neuropil disruption and amyloid deposition (Thal phases) highlighting tau-mediated cytoskeletal collapse as a central driver of neuropil disintegration, this is consistent with recent clinical studies emphasizing tau PET signal as a stronger predictor of cognitive decline than amyloid burden [67, 68].

Despite the early signs of neuropil disruption observed in our cohort, several limitations warrant a cautious interpretation regarding the temporal sequence of pathological events. Specifically, while neuropil alterations were detectable in cases with minimal AT8-positive tau pathology, our current data cannot definitively distinguish whether this reflects a true temporal precedence or is a consequence of differing detection sensitivities and thresholding inherent to immunohistochemical techniques. In that case, whether neuropil disruption precedes the formation of mature neurofibrillary tangles remains further investigation. Future research utilizing more sensitive quantitative assays, such as high-resolution spatial proteomics or ultra-sensitive biochemical validation of tau burden, will be essential to more rigorously delineate the spatiotemporal relationship between structural neuropil fragmentation and the biochemical evolution of tau pathology. Finally, when utilizing our proposed neuropil staging system, it is crucial to recognize that the primary focus of observation and interpretation should be on neuropil pathology. Careful morphological evaluation of neuropil fiber fragmentation is required to distinguish these degenerative features from other concurrently labeled fibrillary structures, particularly intact dendritic and neurofibrillary element, thereby ensuring the high fidelity and reproducibility of this neuropil staging in neuropathological assessments.

Conclusion

This study validates the quantitative assessment of neuropil fibers morphology as a robust indicator of AD pathology. These findings demonstrate that progressive neuritic fiber shortening and increased geometric curvature are intrinsic to the neurodegenerative process, mirroring cytoskeletal fragmentation and correlating strongly with P-tau accumulation. Furthermore, the superior correlation of our novel histological grading

system with Tau load, rather than amyloid-β, reinforces the centrality of cytoskeletal breakdown in AD progression. Building on the framework of plaque and tangle, detecting neuropil alterations in the brain may shed light on a new avenue for the pathological diagnosis of AD. Ultimately, this framework not only deepens the understanding of early AD pathogenesis but also establishes neuropil morphometry as a sensitive, potentially pre-symptomatic biomarker, offering a valuable foundation for the development of next-generation diagnostic strategies and clinical interventions.

Author Contributions

Z.Z., X.W. and C.W. developed the concept and designed the study. Z.Z., X.W. and X.M. performed experiments and data acquisition. Y.W., S.W., Y.P., Y.S, G.T and K.C. conducted data analysis and statistical evaluation. J.Z. contributed to data interpretation and provided organizational support. X.W. and C.W. supervised the project. All authors participated in drafting the manuscript, discussed the results, and approved the final version.

Acknowledgements

We are grateful to National Human Brain Bank for Development and Function (Chinese Academy of Medical Sciences and Peking Union Medical College, Beijing, China), National Health and Disease Human Brain Tissue Resource Center (Anhui Medical University, Hefei, China), Netherlands Brain Bank (Amsterdam, Netherlands) for providing human brain materials and clinical details. This study was supported by the Institute of Basic Medical Sciences, Chinese Academy of Medical Sciences, Neuroscience Center, and the China Human Brain Banking Consortium.

Funding

This work was supported by the STI2030-Major Projects (2022ZD0205202), the Anhui Province University Scientific Research Project (KJ2021A0212, 2022AH0 51169), the Anhui Medical University Research Funding (2021xkj008), the Anhui Medical University Scientific Research Institution Construction and Promotion Plan Fund (2025xkjT014).

Data Availability

No datasets were generated or analyzed during the current study.

Ethical approval

AD human brain paraffin brain sections were obtained from the Netherlands Brain Bank (coordinator: Dr. Inge Huitinga), National Health and Disease Human Brain Tissue Resource Center (Anhui Medical University, Hefei, China) and National Human Brain Bank for Development and Function (Chinese Academy of Medical Sciences and Peking Union Medical College, Beijing, China). The study protocols involving human brain tissue samples were approved by the ethics committee of Anhui Medical University (No. 83244549), ethics committee of the Institute of Basic Medical Sciences, Chinese Academy of Medical Sciences (No. 2022125).

Conflict of Interest

The authors declare no conflict of interest.

Supplementary Materials

The Supplementary data can be found online at: www.aginganddisease.org/EN/10.14336/AD.2026.0213.

References

[1] Scheff SW, Price DA, Schmitt FA, Mufson EJ (2006). Hippocampal synaptic loss in early Alzheimer's disease and mild cognitive impairment. Neurobiol Aging, 27:1372-1384.

[2] Polychronidou E, Avramouli A, Vlamos P (2020). Alzheimer's Disease: The Role of Mutations in Protein Folding. Adv Exp Med Biol, 1195:227-236.

[3] Holtzman DM, Morris JC, Goate AM (2011). Alzheimer's disease: the challenge of the second century. Sci Transl Med, 3:77sr71.

[4] Hirase H, Shinohara Y (2014). Transformation of cortical and hippocampal neural circuit by environmental enrichment. Neuroscience, 280:282-298.

[5] De Lorenzi D, Mandara MT. 2016. The Central Nervous System. In Canine and Feline Cytology. 369-407.

[6] Wang Y, Mandelkow E (2016). Tau in physiology and pathology. Nat Rev Neurosci, 17:5-21.

[7] Braak H, Del Tredici K (2011). The pathological process underlying Alzheimer's disease in individuals under thirty. Acta Neuropathol, 121:171-181.

[8] Zhao D, Zhou Y, Huo Y, Meng J, Xiao X, Han L, et al. (2021). RPS23RG1 modulates tau phosphorylation and axon outgrowth through regulating p35 proteasomal degradation. Cell Death Differ, 28:337-348.

[9] Depp C, Sun T, Sasmita AO, Spieth L, Berghoff SA, Nazarenko T, et al. (2023). Myelin dysfunction drives amyloid-beta deposition in models of Alzheimer's disease. Nature, 618:349-357.

[10] Cai Y, Pinheiro-de-Sousa I, Slobodyanyuk M, Chen F, Huynh T, Kanyo J, et al. (2025). Myelin-axon interface

vulnerability in Alzheimer's disease revealed by subcellular proteomics and imaging of human and mouse brain. Nat Neurosci, 28:1418-1435.
[11] Stokin GB, Goldstein LS (2006). Axonal transport and Alzheimer's disease. Annu Rev Biochem, 75:607-627.
[12] Barthet G, Mulle C (2020). Presynaptic failure in Alzheimer's disease. Prog Neurobiol, 194:101801.
[13] Yuan P, Zhang M, Tong L, Morse TM, McDougal RA, Ding H, et al. (2022). PLD3 affects axonal spheroids and network defects in Alzheimer's disease. Nature, 612:328-337.
[14] Russo ML, Ayala G, Neal D, Rogalsky AE, Ahmad S, Musial TF, et al. (2024). Alzheimer's-linked axonal changes accompany elevated antidromic action potential failure rate in aged mice. Brain Res, 1841:149083.
[15] Walker KA, Duggan MR, Gong Z, Dark HE, Laporte JP, Faulkner ME, et al. (2023). MRI and fluid biomarkers reveal determinants of myelin and axonal loss with aging. Ann Clin Transl Neurol, 10:397-407.
[16] Braak E, Braak H, Mandelkow EM (1994). A sequence of cytoskeleton changes related to the formation of neurofibrillary tangles and neuropil threads. Acta Neuropathol, 87:554-567.
[17] Mirra SS, Heyman A, McKeel D, Sumi SM, Crain BJ, Brownlee LM, et al. (1991). The Consortium to Establish a Registry for Alzheimer's Disease (CERAD). Part II. Standardization of the neuropathologic assessment of Alzheimer's disease. Neurology, 41:479-486.
[18] Montine TJ, Phelps CH, Beach TG, Bigio EH, Cairns NJ, Dickson DW, et al. (2012). National Institute on Aging-Alzheimer's Association guidelines for the neuropathologic assessment of Alzheimer's disease: a practical approach. Acta Neuropathol, 123:1-11.
[19] Therriault J, Zimmer ER, Benedet AL, Pascoal TA, Gauthier S, Rosa-Neto P (2022). Staging of Alzheimer's disease: past, present, and future perspectives. Trends Mol Med, 28:726-741.
[20] Yamamoto T, Hirano A (1986). A comparative study of modified Bielschowsky, Bodian and thioflavin S stains on Alzheimer's neurofibrillary tangles. Neuropathol Appl Neurobiol, 12:3-9.
[21] Gersh I (1953). Histochemistry: Theoretical and Applied. Science, 118:785-785.
[22] Herickhoff L, Stack S, Robertson J (1992). Staining plant cells with silver. III. The mechanism. Biotech Histochem, 67:171-182.
[23] Jay B. Angevine J. 2002. Encyclopedia of the Human Brain. San Diego, Calif: Academic Press.
[24] Jan YN, Jan LY (2010). Branching out: mechanisms of dendritic arborization. Nat Rev Neurosci, 11:316-328.
[25] Suenaga T, Hirano A, Llena JF, Yen SH, Dickson DW (1990). Modified Bielschowsky stain and immunohistochemical studies on striatal plaques in Alzheimer's disease. Acta Neuropathol, 80:280-286.
[26] Gutierrez-Vargas JA, Castro-Alvarez JF, Zapata-Berruecos JF, Abdul-Rahim K, Arteaga-Noriega A (2022). Neurodegeneration and convergent factors contributing to the deterioration of the cytoskeleton in Alzheimer's disease, cerebral ischemia and multiple sclerosis (Review). Biomed Rep, 16:27.
[27] Kanaan NM, Pigino GF, Brady ST, Lazarov O, Binder LI, Morfini GA (2013). Axonal degeneration in Alzheimer's disease: when signaling abnormalities meet the axonal transport system. Exp Neurol, 246:44-53.
[28] Gafson AR, Barthelemy NR, Bomont P, Carare RO, Durham HD, Julien JP, et al. (2020). Neurofilaments: neurobiological foundations for biomarker applications. Brain, 143:1975-1998.
[29] Schmahmann JD, Pandya DN. 2006. Fiber Pathways of the Brain. Oxford, New York: Oxford University Press.
[30] Pakkenberg B, Gundersen HJ (1997). Neocortical neuron number in humans: effect of sex and age. J Comp Neurol, 384:312-320.
[31] Erzurumlu R, Sengul G, Ulupinar E. 2024. Human Neuroanatomy. London, United Kingdom; San Diego, CA: Academic Press.
[32] Konstantopoulos K, Giakoumettis D. 2023. Neuroimaging in Neurogenic Communication Disorders. London, England: Academic Press.
[33] Fellgiebel A, Schermuly I, Gerhard A, Keller I, Albrecht J, Weibrich C, et al. (2008). Functional relevant loss of long association fibre tracts integrity in early Alzheimer's disease. Neuropsychologia, 46:1698-1706.
[34] Vanderlinden G, Radwan A, Christiaens D, Blommaert J, Sunaert S, Vandenbulcke M, et al. (2025). Fibre density and cross-section associate with hallmark pathology in early Alzheimer's disease. Alzheimers Res Ther, 17:73.
[35] Nishioka C, Liang HF, Barsamian B, Sun SW (2019). Amyloid-beta induced retrograde axonal degeneration in a mouse tauopathy model. Neuroimage, 189:180-191.
[36] Serrano-Pozo A, Frosch MP, Masliah E, Hyman BT (2011). Neuropathological alterations in Alzheimer disease. Cold Spring Harb Perspect Med, 1:a006189.
[37] Coleman MP, Hoke A (2020). Programmed axon degeneration: from mouse to mechanism to medicine. Nat Rev Neurosci, 21:183-196.
[38] Stokin GB, Lillo C, Falzone TL, Brusch RG, Rockenstein E, Mount SL, et al. (2005). Axonopathy and transport deficits early in the pathogenesis of Alzheimer's disease. Science, 307:1282-1288.
[39] Vanderlinden G, Koole M, Michiels L, Lemmens R, Vandenbulcke M, Van Laere K (2025). Longitudinal synaptic loss versus tau Braak staging in amnestic mild cognitive impairment. Alzheimers Dement, 21:e14412.
[40] Anton-Fernandez A, Leon-Espinosa G, DeFelipe J, Munoz A (2022). Pyramidal cell axon initial segment in Alzheimer s disease. Sci Rep, 12:8722.
[41] Hahn I, Voelzmann A, Liew YT, Costa-Gomes B, Prokop A (2019). The model of local axon homeostasis - explaining the role and regulation of microtubule bundles in axon maintenance and pathology. Neural Dev, 14:11.
[42] Ballatore C, Lee VM, Trojanowski JQ (2007). Tau-mediated neurodegeneration in Alzheimer's disease and related disorders. Nat Rev Neurosci, 8:663-672.
[43] Bartzokis G (2004). Age-related myelin breakdown: a developmental model of cognitive decline and Alzheimer's disease. Neurobiol Aging, 25:5-18; author reply 49-62.

[44] Braak H, Braak E (1996). Development of Alzheimer-related neurofibrillary changes in the neocortex inversely recapitulates cortical myelogenesis. Acta Neuropathol, 92:197-201.

[45] Seeley WW, Crawford R, Rascovsky K, Kramer JH, Weiner M, Miller BL, et al. (2008). Frontal paralimbic network atrophy in very mild behavioral variant frontotemporal dementia. Arch Neurol, 65:249-255.

[46] Buckner RL, Snyder AZ, Shannon BJ, LaRossa G, Sachs R, Fotenos AF, et al. (2005). Molecular, structural, and functional characterization of Alzheimer's disease: evidence for a relationship between default activity, amyloid, and memory. J Neurosci, 25:7709-7717.

[47] Seeley WW, Crawford RK, Zhou J, Miller BL, Greicius MD (2009). Neurodegenerative diseases target large-scale human brain networks. Neuron, 62:42-52.

[48] de Calignon A, Polydoro M, Suarez-Calvet M, William C, Adamowicz DH, Kopeikina KJ, et al. (2012). Propagation of tau pathology in a model of early Alzheimer's disease. Neuron, 73:685-697.

[49] Ebneth A, Godemann R, Stamer K, Illenberger S, Trinczek B, Mandelkow E (1998). Overexpression of tau protein inhibits kinesin-dependent trafficking of vesicles, mitochondria, and endoplasmic reticulum: implications for Alzheimer's disease. J Cell Biol, 143:777-794.

[50] Castellano JM, Kim J, Stewart FR, Jiang H, DeMattos RB, Patterson BW, et al. (2011). Human apoE isoforms differentially regulate brain amyloid-beta peptide clearance. Sci Transl Med, 3:89ra57.

[51] Tiraboschi P, Hansen LA, Masliah E, Alford M, Thal LJ, Corey-Bloom J (2004). Impact of APOE genotype on neuropathologic and neurochemical markers of Alzheimer disease. Neurology, 62:1977-1983.

[52] Deane R, Sagare A, Hamm K, Parisi M, Lane S, Finn MB, et al. (2008). apoE isoform-specific disruption of amyloid beta peptide clearance from mouse brain. J Clin Invest, 118:4002-4013.

[53] Halliday MR, Pomara N, Sagare AP, Mack WJ, Frangione B, Zlokovic BV (2013). Relationship between cyclophilin a levels and matrix metalloproteinase 9 activity in cerebrospinal fluid of cognitively normal apolipoprotein e4 carriers and blood-brain barrier breakdown. JAMA Neurol, 70:1198-1200.

[54] Halliday MR, Rege SV, Ma Q, Zhao Z, Miller CA, Winkler EA, et al. (2016). Accelerated pericyte degeneration and blood-brain barrier breakdown in apolipoprotein E4 carriers with Alzheimer's disease. J Cereb Blood Flow Metab, 36:216-227.

[55] Shi Y, Yamada K, Liddelow SA, Smith ST, Zhao L, Luo W, et al. (2017). ApoE4 markedly exacerbates tau-mediated neurodegeneration in a mouse model of tauopathy. Nature, 549:523-527.

[56] Terry RD, Masliah E, Salmon DP, Butters N, DeTeresa R, Hill R, et al. (1991). Physical basis of cognitive alterations in Alzheimer's disease: synapse loss is the major correlate of cognitive impairment. Ann Neurol, 30:572-580.

[57] Subramanian J, Savage JC, Tremblay ME (2020). Synaptic Loss in Alzheimer's Disease: Mechanistic Insights Provided by Two-Photon in vivo Imaging of Transgenic Mouse Models. Front Cell Neurosci, 14:592607.

[58] Hojjati SH, Butler TA, de Leon M, Gupta A, Nayak S, Luchsinger JA, et al. (2025). Inter-network functional connectivity increases by beta-amyloid and may facilitate the early stage of tau accumulation. Neurobiol Aging, 148:16-26.

[59] Nathan BP, Bellosta S, Sanan DA, Weisgraber KH, Mahley RW, Pitas RE (1994). Differential effects of apolipoproteins E3 and E4 on neuronal growth in vitro. Science, 264:850-852.

[60] Margeta MA, Yin Z, Madore C, Pitts KM, Letcher SM, Tang J, et al. (2022). Apolipoprotein E4 impairs the response of neurodegenerative retinal microglia and prevents neuronal loss in glaucoma. Immunity, 55:1627-1644 e1627.

[61] Diaz JR, Marta-Ariza M, Khodadadi-Jamayran A, Heguy A, Tsirigos A, Pankiewicz JE, et al. (2022). Apolipoprotein E4 Effects a Distinct Transcriptomic Profile and Dendritic Arbor Characteristics in Hippocampal Neurons Cultured in vitro. Front Aging Neurosci, 14:845291.

[62] Shao X, You R, Hui TH, Fang C, Gong Z, Yan Z, et al. (2019). Tension- and Adhesion-Regulated Retraction of Injured Axons. Biophys J, 117:193-202.

[63] Datar A, Ameeramja J, Bhat A, Srivastava R, Mishra A, Bernal R, et al. (2019). The Roles of Microtubules and Membrane Tension in Axonal Beading, Retraction, and Atrophy. Biophys J, 117:880-891.

[64] Nakayama Y, Aoki Y, Niitsu H (2001). Studies on the mechanisms responsible for the formation of focal swellings on neuronal processes using a novel in vitro model of axonal injury. J Neurotrauma, 18:545-554.

[65] Roy S, Zhang B, Lee VM, Trojanowski JQ (2005). Axonal transport defects: a common theme in neurodegenerative diseases. Acta Neuropathol, 109:5-13.

[66] Miyasaka T, Sato S, Tatebayashi Y, Takashima A (2010). Microtubule destruction induces tau liberation and its subsequent phosphorylation. FEBS Lett, 584:3227-3232.

[67] Sperling RA, Donohue MC, Rissman RA, Johnson KA, Rentz DM, Grill JD, et al. (2024). Amyloid and Tau Prediction of Cognitive and Functional Decline in Unimpaired Older Individuals: Longitudinal Data from the A4 and LEARN Studies. J Prev Alzheimers Dis, 11:802-813.

[68] Groot C, Smith R, Collij LE, Mastenbroek SE, Stomrud E, Binette AP, et al. (2024). Tau Positron Emission Tomography for Predicting Dementia in Individuals With Mild Cognitive Impairment. JAMA Neurol, 81:845-856.